May 2020

Selective Actuation and Sensing of Antisymmetric Lamb Wave Mode Using D15 Piezoelectric Transducers

Parry Carrison
University of Wisconsin-Milwaukee

SELECTIVE ACTUATION AND SENSING OF ANTISYMMETRIC LAMB WAVE MODE USING D_{15} PIEZOELECTRIC TRANSDUCERS

by

Parry Carrison

A Thesis Submitted in

Partial Fulfillment of the

Requirements for the Degree of

Master of Science

in Engineering

at

The University of Wisconsin-Milwaukee

May 2020

ABSTRACT

SELECTIVE ACTUATION AND SENSING OF ANTISYMMETRIC LAMB WAVE MODE USING D_{15} PIEZOELECTRIC TRANSDUCERS

by

Parry Carrison

The University of Wisconsin-Milwaukee, 2020
Under the Supervision of Professor Nathan Salowitz

ABSTRACT

Undetected damage in aircraft can lead to catastrophic failures and loss of life. Automated embedded damage detection systems can reduce manhours and downtime due to inspection. Ultrasonic inspection has become one of the most capable methods for thin plate-like structures, such as aircraft spars, stiffeners, and skins. Piezoelectric transducers can inspect structures by generating ultrasonic Lamb waves and sensing how they propagate. Many Lamb wave modes exist at a given frequency, which makes signal interpretation challenging. Selective actuation of a single mode simplifies the signal analysis. The A_0 mode has the shortest wavelength, which increases sensitivity to small defects, and its group velocity is independent of composite structure layup. Recent research has found a shear-mode d_{15} piezoelectric transducer will selectively actuate the A_0 mode when embedded at the neutral axis of a composite structure. Precise placement of the transducer at the neutral axis is difficult due to operator error, changing manufacturing environments, and design constraints. This work studies the relationship between off-axis d_{15} transducer placement and A_0 mode selectivity through analytical, numerical, and experimental methods. A_0 selectivity was found to be 12.7 dBV at the neutral axis but dropped 4.02 dBV when moved off-axis by 5.5% of the structure thickness, a drop of approximately 0.73 dBV/% of structure's thickness from the neutral axis.

TABLE OF CONTENTS

LIST OF FIGURES

LIST OF TABLES

ACKNOWLEDGEMENTS

I would like to thank my advisor Professor Nathan Salowitz for his support and encouragement in completing this thesis. I would also like to thank my colleagues in the Advanced Structures Laboratory at UW-Milwaukee for sharing their research interests with me. Above all, I'd like to thank my wife for the support she has given me for the past few years as I've completed this work.

1.0 Introduction

The objective of this work was to study the effect of the through thickness position of shear-mode d_{15} piezoelectric transducers in plate-like structures on actuation and sensing of different Lamb wave modes. This work was intended to determine the effect of transducer placement relative to the neutral axis on A_0 selectivity. The findings of this work provide insight to practitioners of Structural Health Monitoring.

Structural Health Monitoring (SHM) is the use of automated and embedded systems to determine the physical condition of a structure [1]. A typical SHM system uses a network of sensors that measure parameters which are relevant to the state of the structure and its environment. These autonomous built-in systems enable continuous real-time monitoring, inspection, and damage detection of structures with minimal labor and provide a high level of confidence and reliability.

Many applications of SHM are found in the aerospace and civil engineering industries. SHM can greatly reduce downtime and maintenance costs in the aerospace industry by allowing real-time inspection of hard to access locations. For example, aircraft spars and stiffeners are difficult to access, because once the aircraft is built, they are covered with the fuselage or wing skin. In 2006, Boeing indicated that most inspection expenses are due to difficulty accessing inspection areas [2]. The 747-400 undergoes 25,000 hours of corrosion inspection during its lifetime, with 21,000 of those hours spent gaining access to hard-to-reach areas. SHM shows promise of monitoring structural condition throughout aircraft service lifetime [3]. SAE has published guidelines for implementing SHM in fixed wing aircraft in [4]. More applications of SHM to aircraft are explored in [5].

SHM is one of the most powerful management tools in the civil engineering community, according to Inaudi and Glisic [6]. Defects were identified in a railway turnout by Wang et al [7] using piezoelectric wafer active sensors (PWAS). Ciang, Lee, and Bang highlight the potential applications of SHM for wind turbines in [8]. SHM of bridges has seen a large acceptance in Asia. Mao identified 31 bridges in China which have been instrumented since 2008, each with an average of 250 sensors [9]. An array of 11 PWAS was used by Zhu and Rizzo [10] to identify cracks in a truss structure. PWAS could potentially monitor loss of wall thickness in pipeline due to corrosion, as demonstrated by Na [11]. PWAS were used by Tua et al. [12] to detect and locate cracks 200 microns wide in aluminum pipes buried in sand.

Some current SHM systems use electrical impedance tomography (EIT), ultrasonic methods, and strain mapping. EIT is based on injecting a known amount of current into the system at multiple points and measuring the voltage drop, in order map the electrical conductivity. By knowing the nominal conductivity of the material, one can locate and detect damage. However, current implementations rely on large external probes. Likewise, SHM methods that rely on bulk ultrasonic waves require large wedge transducers, which are not conducive to in situ monitoring. Strain mapping involves measurement of a structure's strain field over time, and allows for detection, location, and quantification of the extent of damage. In situ monitoring is achievable with a network of cheap strain gauges, however, each gauge can only measure local strain field, thus limiting the practicality of this method for inspecting large structures.

Some advantages over these systems are achieved through guided ultrasonic wave inspection with inexpensive piezoelectric wafer active sensors (PWAS). PWAS investigate a structure by generating and sensing an ultrasonic guided wave, called a Lamb wave. Unlike bulk ultrasonic waves, Lamb waves are confined to the boundaries of the structure. The generated Lamb waves interact with defects, and the altered waves are sensed and analyzed to detect, locate, and predict the size and type of defect. Lamb waves often occur in thin plates and shell structures. They consist of superposition of longitudinal and shear elastic waves. Lamb waves can propagate over long distances, and can locate small defects such as cracks, delamination, and local changes in wall thickness from only a few monitoring points. They also allow inspection of the structure's full cross-sections. Lamb waves have multiple modes of deformation, which can coexist at any frequency. These are the symmetric modes (denoted S_0, S_1, S_2, etc.) and the antisymmetric modes (denoted A_0, A_1, A_2, etc.).

Signal analysis can be simplified by selectively actuating only one Lamb wave mode. Selective excitation of the A_0 Lamb wave mode offers some advantages in particular. The A_0 mode has a shorter wavelength than S_0, which increases sensitivity to small defects and resolution of measurements. The A_0 mode has also been shown to be particularly sensitive to delamination and transverse ply cracks [13] [14] [15]. The group velocity of the A_0 mode has been shown to be insensitive to composite layup and can be closely approximated with bulk laminate properties [16]. Unlike the S_0 mode, signal attenuation of the A_0 mode scales linearly with frequency. Also, the A_0 mode group velocity and wave amplitude has been shown to be insensitive to thick surface coatings (greater than 1 mm) [17].

Some methods to selectively actuate the A_0 mode with PZTs have been studied in the past. Surface-mounted d_{31} piezoelectric lead zirconate titanate transducers (PZT) will selectively actuate the A_0 or S_0 modes depending on the wavenumber associated with the actuation frequency and the PZT length, as discussed by Giugiutiu in [18]. A pair of d_{31} PZTs mounted on the same surface, spaced by an integer multiple of the A_0 mode wavelength, and actuated in phase were found to selectively actuate the A_0 mode by Grondel et al. [19]. A high purity A_0 mode transducer consisting of a d_{31} PZT, a Pz27 (Ferro-perm, Kvistgard, Denmark) front layer, and brass backing mass was developed by Cawley et al. [20].

Recent research has found shear mode d_{15} PZTs embedded within the structure have an inherent advantage over d_{31} PZTs in selectively actuating the A_0 wave. Antisymmetric deformation is coupled to shear strain through classical beam theory [21]. By applying shear strain directly to the neutral axis of a structure, antisymmetric deformation can be maximized without introducing symmetric (axial) deformation to the structure, whereas surface-mounted d_{31} PZTs introduce both symmetric and antisymmetric deformation. Another benefit is that embedding the PZTs provides some protection from the service environment, improving the durability of the measurement system [22]. Embedding causes only slight degradation of the host material's mechanical properties, as discussed in [23] [24].

Additional findings on the properties of embedded d_{15} PZTs are summarized here:

1. The interface stress between embedded d_{15} PZTs and the structure is significantly lower than that of surface mounted d_{31} PZTs [25].
2. Shear mode d_{15} PZTs embedded in a cantilevered beam produce a larger tip displacement than surface-mounted d_{31} PZTs for a given electric field strength [25] [26] (up to a PZT length-to-thickness ratio of 10).
3. The longitudinal stress in an electrically actuated d_{15} PZT embedded at the neutral axis is significantly lower than that of surface mounted d_{31} PZTs [27].
4. Shear mode d_{15} PZTs embedded at the neutral axis selectively actuate and sense the A_0 mode [28].

5. When a d_{15} PZT is sandwiched between two plates, the neutral axis is the optimal position to induce out-of-plane deflection [29] [30].

The purpose of this work is to investigate A_0 actuation selectivity using d_{15} PZT transducers when the actuator is off the neutral axis. The work begins with an examination of the theory of elastic waves. It continues with the theory of Lamb waves. Analytical equations are derived to describe a shear-mode PZT embedded inside a structure. A finite element (FE) parametric study is conducted to consider selectivity as a function of d_{15} PZT position and actuation frequency.

Models and experiments confirmed that the shear-mode d_{15} PZT located at the neutral axis will selectively actuate the A_0 Lamb wave mode. Selectivity decreases as the actuator is moved from the neutral axis. However, surface-mounted d_{31} PZTs were found to produce larger actuation strains than the neutral-axis d_{15} PZT, and to produce larger sensing voltages than the neutral-axis d_{15} PZT. Nevertheless, the d_{15} PZT showed 12.7 dBV A_0/S_0 selectivity when located at the neutral axis and lost 4.02 dBV when moved 5.5% of the sample thickness away from the neutral axis, a drop rate of 0.73 dBV/%.

2.0 Elastic Wave Potentials

Before considering Lamb waves, it is necessary to discuss elastic wave theory. The displacement induced by a wave can be expressed in terms of two potential functions. These are the scalar potential Φ, and the vector potential $\vec{H} = H_x\vec{i} + H_y\vec{j} + H_z\vec{k}$. The potentials representation of the displacement field is shown below.

$$\vec{u} = \vec{\nabla}\Phi + \vec{\nabla} \times \vec{H} \tag{1}$$

A particularly interesting case is that of straight-crested, z-invariant waves. The wave is constant in the z direction. These straight-crested waves will be shown to give rise to Lamb waves. For a z-invariant condition, the following simplifications apply.

$$\frac{\partial}{\partial z} \equiv 0 \quad \text{and} \quad \vec{\nabla} = \vec{i}\frac{\partial}{\partial x} + \vec{j}\frac{\partial}{\partial y} \tag{2}$$

Substitution of the equation 2 into equation 1 yields the following.

$$\vec{u} = \left(\frac{\partial \Phi}{\partial x} + \frac{\partial H_z}{\partial y}\right)\vec{i} + \left(\frac{\partial \Phi}{\partial y} - \frac{\partial H_z}{\partial x}\right)\vec{j} + \left(\frac{\partial H_y}{\partial x} - \frac{\partial H_x}{\partial y}\right)\vec{k} \tag{3}$$

Equation 3 shows that the problem still yields displacement in all 3 directions, even though the problem is z-invariant. The solution can be split into two cases. One case describes the motion due to H_x and H_y, in which u_z is non-zero, while u_x and u_y are zero. This case describes shear motion in the horizontal plane. These waves are called shear horizontal waves, or SH waves. The second case describes motion due to Φ and H_z, in which u_x and u_y are non-zero, while u_z is zero. This case describes motion from a pressure wave, or P-wave, due to the potential Φ, as well as motion from a shear vertical wave, or SV-wave, due to the potential H_z. This case is also called the P + SV solution.

A useful simplification of the 3D stress-strain relations can be found by making use of the Lamé constants λ and μ. These are:

$$\lambda = \frac{\nu}{(1+\nu)(1-2\nu)}E \qquad\qquad \mu = G = \frac{1}{2(1+\nu)}E \tag{4}$$

Where E, G, and ν are the Young's modulus of elasticity, shear modulus, and Poisson's ratio respectively. The 3D stress-strain relations can then be described as:

$$
\begin{aligned}
\sigma_{xx} &= (\lambda+2\mu)\frac{\partial u_x}{\partial x} + \lambda\frac{\partial u_y}{\partial y} + \lambda\frac{\partial u_z}{\partial z} & \sigma_{xy} &= \mu\left(\frac{\partial u_x}{\partial y} + \frac{\partial u_y}{\partial x}\right) \\
\sigma_{yy} &= \lambda\frac{\partial u_x}{\partial x} + (\lambda+2\mu)\frac{\partial u_y}{\partial y} + \lambda\frac{\partial u_z}{\partial z} & \sigma_{yz} &= \mu\left(\frac{\partial u_y}{\partial z} + \frac{\partial u_z}{\partial y}\right) \\
\sigma_{zz} &= \lambda\frac{\partial u_x}{\partial x} + \lambda\frac{\partial u_y}{\partial y} + (\lambda+2\mu)\frac{\partial u_z}{\partial z} & \sigma_{zx} &= \mu\left(\frac{\partial u_z}{\partial x} + \frac{\partial u_x}{\partial z}\right)
\end{aligned}
\tag{5}
$$

We are interested in the case of P + SV waves. We know that u_z and $\frac{\partial}{\partial z}$ are zero for this case. Substitution of the components of equation 3 into equation 5 yields:

$$
\begin{aligned}
\sigma_{xx} &= \lambda\left(\frac{\partial^2\Phi}{\partial x^2} + \frac{\partial^2\Phi}{\partial y^2}\right) + 2\mu\left(\frac{\partial^2\Phi}{\partial x^2} + \frac{\partial^2 H_z}{\partial x\,\partial y}\right) \\
\sigma_{yy} &= \lambda\left(\frac{\partial^2\Phi}{\partial x^2} + \frac{\partial^2\Phi}{\partial y^2}\right) + 2\mu\left(\frac{\partial^2\Phi}{\partial y^2} - \frac{\partial^2 H_z}{\partial x\,\partial y}\right) \\
\sigma_{zz} &= \lambda\left(\frac{\partial^2\Phi}{\partial x^2} + \frac{\partial^2\Phi}{\partial y^2}\right) \\
\sigma_{xy} &= \mu\left(2\frac{\partial^2\Phi}{\partial x\,\partial y} - \frac{\partial^2 H_z}{\partial x^2} + \frac{\partial^2 H_z}{\partial y^2}\right)
\end{aligned}
\tag{6}
$$

3.0 Derivation of Lamb Wave Equations

We will begin by considering straight-crested, z-invariant Lamb waves propagating in a plate of thickness $h = 2d$ (see Figure 1). The x axis is aligned with the axial direction of the plate, while the y axis is aligned normal to the plate. Straight crested waves can be split into two separate cases, (1) SH waves or shear horizontal waves, and (2) P + SV waves, or pressure and shear vertical waves, respectively. We are primarily concerned with the P + SV waves. We will assume that P-waves and SV-waves exist simultaneously in the plate. The P-waves and SV-waves reflect off plates lower and upper surfaces. Constructive and destructive interference of these waves create the Lamb waves. Lamb waves consist of a pattern of standing waves in the y direction, which travel in the x direction.

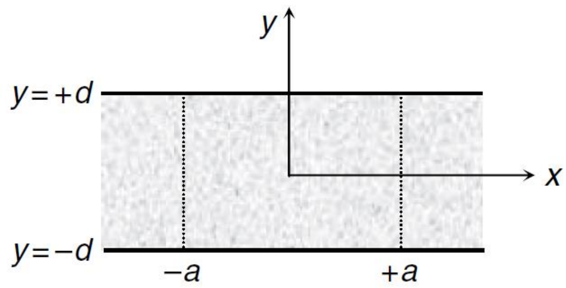

Figure 1: Plate of thickness 2d, with a PWAS of width 2a, under harmonic loading on the top surface. From [31].

The P + SV waves can be described in terms of two scalar potentials, Φ and H_z. The potentials satisfy the wave equation below.

$$\begin{gathered} c_p^2 \nabla^2 \Phi = \ddot{\Phi} \\ c_s^2 \nabla^2 H_z = \ddot{H}_z \end{gathered} \tag{7}$$

Here, c_p and c_s are the pressure and shear wave speeds. It is assumed that the wave excitation is harmonic. Thus,

$$\begin{gathered} \ddot{\Phi} = -\omega^2 \Phi \\ \ddot{H}_z = -\omega^2 H_z \end{gathered} \tag{8}$$

To simplify notation, the rest of the analysis will use φ and ψ in place of Φ and H_z. If we expand the ∇ operator in equation 7, and substitute in equation 8, we find equation 9, the Helmholtz equations for pressure and shear potentials.

$$\begin{gathered} \frac{\partial^2 \phi}{\partial x^2} + \frac{\partial^2 \phi}{\partial y^2} + \frac{\omega^2}{c_P^2}\phi = 0 \\ \frac{\partial^2 \psi}{\partial x^2} + \frac{\partial^2 \psi}{\partial y^2} + \frac{\omega^2}{c_S^2}\psi = 0 \end{gathered} \tag{9}$$

For harmonic motion in the x direction of the form $e^{i(\xi x - \omega t)}$, equation 6 becomes:

$$\begin{gathered} \frac{d^2 \phi}{d y^2} + \left(\frac{\omega^2}{c_P^2} - \xi^2\right)\phi = 0 \\ \frac{d^2 \psi}{d y^2} + \left(\frac{\omega^2}{c_S^2} - \xi^2\right)\psi = 0 \end{gathered} \tag{10}$$

$$u_x = i\xi\phi + \frac{\mathrm{d}\psi}{\mathrm{d}y}, \quad u_y = \frac{\mathrm{d}\phi}{\mathrm{d}y} - i\xi\psi, \quad \varepsilon_x = i\xi u_x$$
$$\tau_{yx} = \mu\left(2i\xi\frac{\mathrm{d}\phi}{\mathrm{d}y} + \xi^2\psi + \frac{\partial^2\psi}{\partial y^2}\right), \quad \tau_{yy} = \lambda\left(-\xi^2\phi + \frac{\mathrm{d}^2\phi}{\mathrm{d}y^2}\right) + 2\mu\left(\frac{\mathrm{d}^2\phi}{\mathrm{d}y^2} - i\xi\frac{\mathrm{d}\psi}{\mathrm{d}y}\right) \tag{11}$$

We introduce the following notations for simplification.

$$\eta_p^2 = \frac{\omega^2}{c_p^2} - \xi^2 \qquad \eta_s^2 = \frac{\omega^2}{c_s^2} - \xi^2 \tag{12}$$

Substitution into equation 10 yields

$$\frac{d^2\Phi}{dy^2} + \eta_p^2\Phi = 0 \qquad \frac{d^2\Psi}{dy^2} + \eta_s^2\Psi = 0 \tag{13}$$

General solutions to equation 13 are

$$\Phi = A_1 \sin\eta_p y + A_2 \cos\eta_p y \tag{14}$$

$$\Psi = B_1 \sin\eta_s y + B_2 \cos\eta_s y$$

Substitution of 14 into the expressions of u_x and u_y in equation 11 yields

$$u_x = i\xi\left(A_1 \sin\eta_p y + A_2 \cos\eta_p y\right) + \eta_s\left(B_1 \cos\eta_s y - B_2 \sin\eta_s y\right) \tag{15}$$

$$u_y = \eta_p\left(A_1 \cos\eta_p y - A_2 \sin\eta_p y\right) - i\xi\left(B_1 \sin\eta_s y + B_2 \cos\eta_s y\right)$$

The partial derivatives of the potentials with respect to y are given as

$$\frac{d\Phi}{dy} = A_1\eta_p \cos\eta_p y - A_2\eta_p \sin\eta_p y \qquad \frac{d\Psi}{dy} = B_1\eta_s \cos\eta_s y - B_2\eta_s \sin\eta_s y \tag{16}$$

$$\frac{d^2\Phi}{dy^2} = -A_1\eta_p^2 \sin\eta_p y - A_2\eta_p^2 \cos\eta_p y = -\eta_p^2\Phi \qquad \frac{d^2\Phi}{dy^2} = -B_1\eta_s^2 \sin\eta_s y - B_2\eta_s^2 \cos\eta_s y = -\eta_s^2\Phi$$

Substitution of equation 16 into the expressions of τ_{yx} and τ_{yy} in equation 11 yields

$$\tau_{xy} = \mu\left[-A_2 2i\xi\eta_p \sin\eta_p y + B_1(\xi^2 - \eta_s^2)\sin\eta_s y + A_1 2i\xi\eta_p \cos\eta_p y + B_2(\xi^2 - \eta_s^2)\cos\eta_s y\right] \tag{17}$$

$$\tau_{yy} = \mu\left[A_2(\xi^2 - \eta_s^2)\cos\eta_p y - B_1 2i\xi\eta_s \cos\eta_s y + A_1(\xi^2 - \eta_s^2)\sin\eta_p y + B_2 2i\xi\eta_s \sin\eta_s y\right]$$

The four constants A_1, A_2, B_1, and B_2 must be found by applying boundary conditions. Lamb waves result in both symmetric and antisymmetric motion with respect to the midplane. Figure 2 illustrates both types of motion. To simplify the solution, we will split the remainder of the analysis into symmetric and antisymmetric solutions.

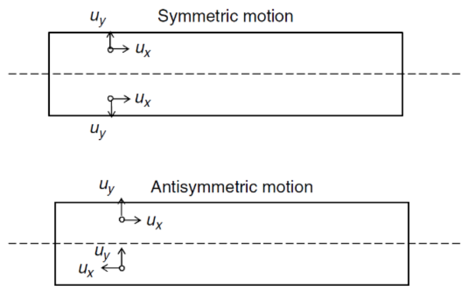

Figure 2: Symmetric and antisymmetric motion in a thin plate. From [31]

3.1 Symmetric Solution

The displacement in the symmetric solution is symmetric about the midplane. This results in the following relations.

$$\begin{aligned} u_x(x,-d) &= u_x(x,d) \qquad & \tau_{yx}(x,-d) &= -\tau_{yx}(x,d) \\ u_y(x,-d) &= -u_y(x,d) \qquad & \tau_{yy}(x,-d) &= \tau_{yy}(x,d) \end{aligned} \tag{18}$$

Notice that u_x is in the same direction on the top and bottom halves of the structure, while u_y is in the opposite direction. Thus, the displacements and potentials can be described as the following for the symmetric solution.

$$\begin{aligned} u_x &= A_2 i\xi \cos\eta_p y + B_1\eta_s \cos\eta_s y \qquad & \Phi &= A_2 \cos\eta_p y \\ u_y &= -A_2\eta_p \sin\eta_p y - B_1 i\xi \sin\eta_s y \qquad & \Psi &= B_1 \sin\eta_s y \end{aligned} \tag{19}$$

Substitution of equation 19 into equation 17 yields the following.

$$\begin{aligned} \tau_{xy} &= \mu\left[-A_2 2i\xi\eta_p \sin\eta_p y + B_1(\xi^2 - \eta_s^2)\sin\eta_s y\right] \\ \tau_{yy} &= \mu\left[A_2(\xi^2 - \eta_s^2)\cos\eta_p y - B_1 2i\xi\eta_s \cos\eta_s y\right] \end{aligned} \tag{20}$$

The boundary conditions for the symmetric solution are

$$\tau_{yx}(x,-d) = -\tau_{yx}(x,d) = 0$$
$$\tau_{yy}(x,-d) = \tau_{yy}(x,d) = 0 \tag{21}$$

Substitution of equation 21 into equation 20 yields the following system of equations.

$$-A_2 2i\xi\eta_p \sin\eta_p d + B_1(\xi^2 - \eta_s^2)\sin\eta_s d = 0 \tag{22}$$

$$A_2(\xi^2 - \eta_s^2)\cos\eta_p d - B_1 2i\xi\eta_s \cos\eta_s d = 0$$

Solution of the system of equations is only possible if its determinant is zero. Therefore,

$$D_s = (\xi^2 - \eta_s^2)^2 \cos\eta_p d \sin\eta_s d + 4\xi^2\eta_p\eta_s \sin\eta_p d \cos\eta_s d = 0 \tag{23}$$

This is the Rayleigh-Lamb equation for symmetric modes. An analytical solution is not readily obtained, because η_p and η_s are dependent on ξ. Therefore, a numerical solution is necessary. Several eigenvalues are obtained, and denoted ξ_0^s, ξ_1^s, ξ_2^s, etc. The dispersive wave speed *c* is a function of the frequency-thickness product *fd*, where *f* is the frequency and *d* is the plate half-thickness. Each eigenvalue yields a separate curve, representing a different symmetric Lamb wave mode, each with a different relationship between dispersive wave speed c and frequency-thickness product. At any given frequency-thickness product, several Lamb wave modes may exist. However, at low values of fd, only the S_0 mode is present. A plot of the dispersive wave speed for symmetric modes in a 3 mm thick aluminum plate is shown in Figure 3.

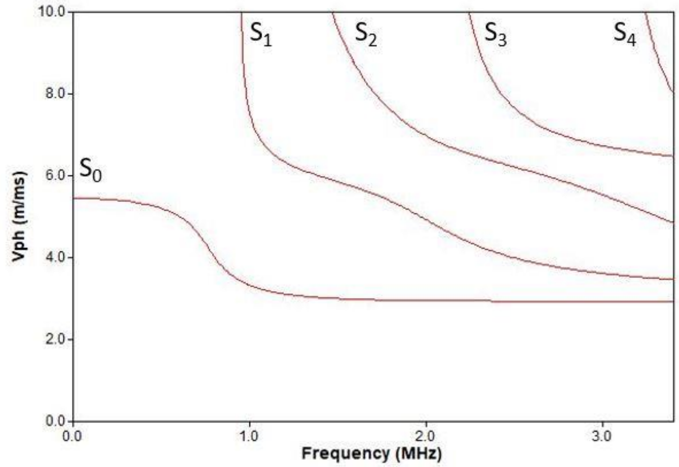

Figure 3: Wave speed dispersion curves for symmetric Lamb wave modes in 3mm thick aluminum plate

Substitution of the eigenvalues into equation 22 yields the coefficients

$$A_2 = 2i\xi\eta_s \cos\eta_s d \tag{24}$$

$$B_1 = (\xi^2 - \eta_s^2)\cos\eta_p d$$

Substitution of equation 24 into the expressions of u_x and u_y in equation 19 yields

$$u_x = -2\xi^2\eta_s \cos\eta_s d \cos\eta_p y + \eta_s(\xi^2 - \eta_s^2)\cos\eta_p\, d \cos\eta_s y \tag{25}$$

$$u_y = -2i\xi\eta_p\eta_s \cos\eta_s d \sin\eta_p y - i\xi(\xi^2 - \eta_s^2)\cos\eta_p\, d \sin\eta_s y$$

The shape of the displacement from an S_0 wave is shown in Figure 4.

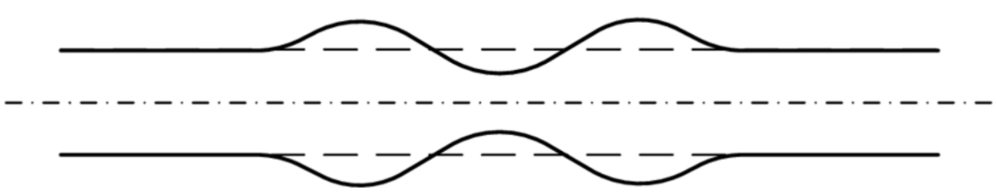

Figure 4: Shape of the S_0 lamb wave mode. From [31].

3.2 Antisymmetric Solution

The displacement in the antisymmetric solution is antisymmetric about the midplane. This results in the following relations.

$$u_x(x,-d) = -u_x(x,d) \qquad \tau_{yx}(x,-d) = \tau_{yx}(x,d) \tag{26}$$
$$u_y(x,-d) = u_y(x,d) \qquad \tau_{yy}(x,-d) = -\tau_{yy}(x,d)$$

Notice that u_y is in the same direction on the top and bottom halves of the structure, while u_x is in the opposite direction. Thus, the displacements and potentials can be described as the following for the antisymmetric solution.

$$u_x = A_1 i\xi \sin\eta_p y - B_2\eta_s \sin\eta_s y \qquad \Phi = A_1 \sin\eta_p y \tag{27}$$

$$u_y = A_1\eta_p \cos\eta_p y - B_2\, i\xi \cos\eta_s y \qquad \Psi = B_2 \cos\eta_s y$$

Substitution of equation 27 into equation 17 yields the following.

$$\tau_{xy} = \mu\left[A_1 2i\xi\eta_p\, cos\,\eta_p y + B_2(\xi^2-\eta_s^2)\, cos\,\eta_s y\right] \tag{28}$$

$$\tau_{yy} = \mu\left[A_1(\xi^2-\eta_s^2)\sin\eta_p y + B_2 2i\xi\eta_s \sin\eta_s y\right]$$

The boundary conditions for the antisymmetric solution are

$$\tau_{yx}(x,-d) = \tau_{yx}(x,d) = 0 \tag{29}$$
$$\tau_{yy}(x,-d) = -\tau_{yy}(x,d) = 0$$

Substitution of equation 29 into equation 28 yields the following system of equations.

$$A_1 2i\xi\eta_p \cos\eta_p d + B_2(\xi^2-\eta_s^2)\cos\eta_s d = 0 \tag{30}$$

$$A_1(\xi^2-\eta_s^2)\sin\eta_p d + B_2 2i\xi\eta_s \sin\eta_s d = 0$$

Solution of the system of equations is only possible if its determinant is zero. Therefore,

$$D_A = (\xi^2-\eta_s^2)^2\sin\eta_p d\cos\eta_s d + 4\xi^2\eta_p\eta_s\cos\eta_p d\sin\eta_s d = 0 \tag{31}$$

This is the Rayleigh-Lamb equation for antisymmetric modes. Like the symmetric problem, an analytical solution is not readily obtained, because η_p and η_s are dependent on ξ. Therefore, a numerical solution is necessary. Several eigenvalues are obtained, and denoted ξ_0^A, ξ_1^A, ξ_2^A, etc. Each eigenvalue yields a separate curve, representing a different antisymmetric Lamb wave mode, each with a different relationship between dispersive wave speed c and frequency-thickness product. At any given frequency-thickness product, several Lamb wave modes may exist. However, at low values of fd, only the A_0 mode is present. A plot of the dispersive wave speed for antisymmetric modes is shown in Figure 5.

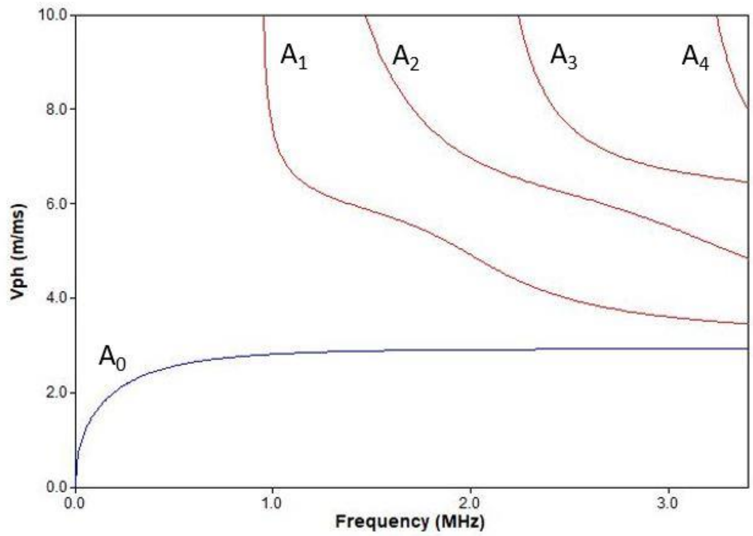

Figure 5: Wave speed dispersion curves for antisymmetric Lamb wave modes in 3mm thick aluminum plate

Substitution of the eigenvalues into equation 30 yields the coefficients

$$A_1 = 2i\xi\eta_s \sin\eta_s d \tag{32}$$

$$B_2 = -(\xi^2 - \eta_s^2)\sin\eta_p d$$

Substitution of equation 32 into the expressions of u_x and u_y in equation 27 yields

$$u_x = -2\xi^2\eta_s \sin\eta_s d \sin\eta_p y + \eta_s(\xi^2 - \eta_s^2)\sin\eta_p d \sin\eta_s y \tag{33}$$

$$u_y = 2i\xi\eta_p\eta_s \sin\eta_s d \cos\eta_p y + i\xi(\xi^2 - \eta_s^2)\sin\eta_p d \cos\eta_s y$$

The shape of the displacement from an A_0 wave is shown in Figure 6.

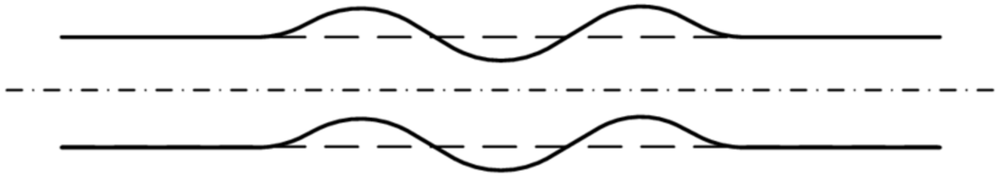

Figure 6: Shape of the A_0 lamb wave mode. From [31].

The through-thickness displacement for the S_0 and A_0 modes is plotted in Figure 7. Notice that there is zero x displacement at the mid-thickness plane for the A_0 mode. Similarly, there is zero y displacement at the mid-thickness plane for the S_0 mode.

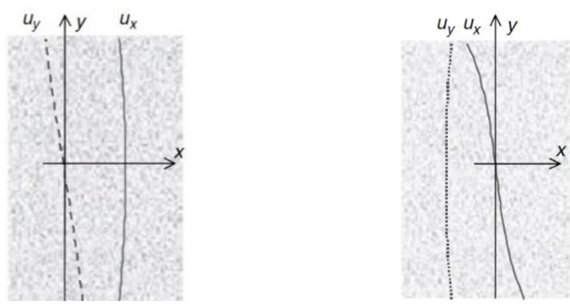

Figure 7: Through-thickness x and y displacement. (Left) S_0 mode (Right) A_0 mode. Adapted from [23].

At low frequency-thickness product, only the A_0 and S_0 modes exist. In this region, any x displacement at the mid-thickness plane can be attributed solely to the S_0 mode, while any y displacement can be attributed solely to the A_0 mode. This feature will become more relevant later, during the interpretation of simulation results.

4.0 d_{15} Actuation and Sensing Selectivity versus PZT location

A theoretical model was created to study the actuation and sensing properties of d_{15} PZT transducers embedded within laminate structures. Experimental and finite element analyses were performed to compare with theory. The theoretical and simulated geometry consisted of two d_{15} PZTs embedded in a solid aluminum beam. The test geometry consisted of two d_{15} PZTs sandwiched between two 1-mm thick aluminum sheets. The aluminum sheets were machined to a size of 305mm x 15mm x 1mm. The d_{15} PZTs were placed 130 mm apart with their poling direction aligned with the length of the aluminum sheets. These sheets were bonded together with a layer of Hysol EA 9394 epoxy (Bay Point, CA, USA) [32]. A d_{31} PZT was mounted on the structural surface adjacent to each d_{15} transducer. Simulation was used to perform a parametric study on the effects of varying the actuation frequency and the distance of the d_{15} actuator from the neutral axis of the structure on the signal strength of the A_0 and S_0 Lamb wave modes.

4.1 Analytical Approach

4.1.1 Analysis of Free Body Piezoelectric Transducers

A theoretical analysis was conducted to establish the relationship between actuation frequency, d_{15} actuator distance from the neutral axis, and A_0 mode selectivity. This began by creating a free body diagram of the laminated structure and a PZT embedded at the neutral axis. Figure 8 shows a d_{15} PZT, with half-thickness *b*, half-length *a*, and unit width. The PZT is polarized in the 1 direction, which is aligned with the y axis. When a voltage is applied across terminals in the y direction, a shear strain γ is created. The shear force F is transferred to the structure. The A_0 wave is a result of a net moment transferred to the structure by the piezoelectric actuator.

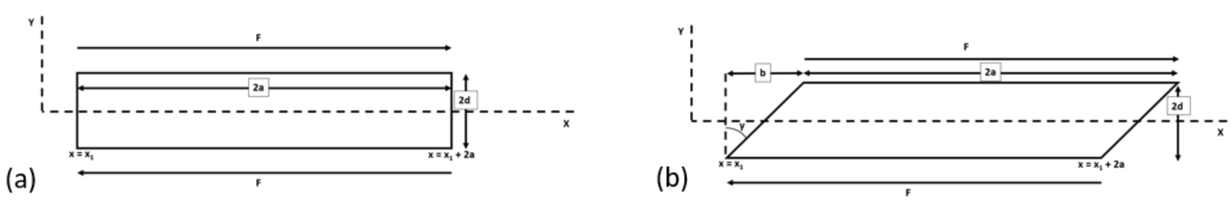

Figure 8: Free body diagram of embedded PZT (a) undeformed (b) after quasi-static deformation

From observation of Figure 8(a), there is a net zero force in the x direction for the undeformed case because the shear force on the top and bottom of the PZT cancel. However, in the quasi-statically deformed case 7(b), the small deflection *b* of the PZT causes the forces to no longer overlap, and an axial force is produced. The axial force is expressed in equation 34.

$$F_x(x) = F\big(-H(x-x_1) + H(x-x_1-b) + H(x-x_1-2a) - H(x-x_1-b-2a)\big) \quad (34)$$

Here, H(x) is the Heaviside step function. It is believed that this small axial force is the source of S_0 actuation in the structure, though it is very small relative to A_0 actuation. A_0 actuation is caused by a moment induced about the z axis. A sum of moments about the z axis yields equation 35.

$$M_z(x) = Fd\big(-H(x-x_1) + H(x-x_1-2a)\big) \quad (35)$$

A similar free body diagram was created to analyze the case of a PZT mounted off the neutral axis. Figure 9 shows a d_{15} PZT, with half-thickness *b*, half-length *a*, and unit width. The PZT is polarized in the 1 direction, which is aligned with the y axis. When a voltage is applied across terminals in the y direction, a shear strain γ is created. The shear force F is transferred to the structure.

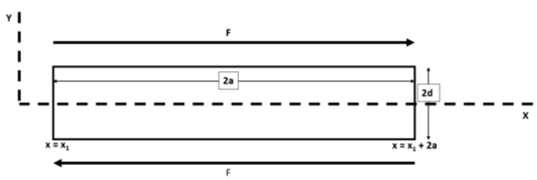

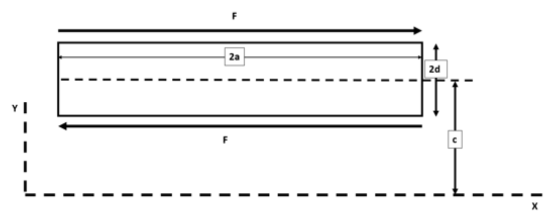

Figure 9: d_{15} actuator (a) on neutral axis, (b) off neutral axis

Equation 36 is a result of the sum of moments about the Z axis.

$$M_z(x) = [F(c-d) - F(c+d)]\big(-H(x-x_1) + H(x-x_1-2a)\big) \quad (36)$$

Equation 36 simplifies to equation 37.

$$M_z(x) = Fd\big(-H(x-x_1) + H(x-x_1-2a)\big) \quad (37)$$

This equation is equivalent to equation 35, describing the moment created for the case of an actuator on the neutral axis. It is clear that the variable *c*, representing the distance of the d_{15} actuator from the neutral axis, is not in the equation. In other words, actuation of the A_0 mode is independent of the position of the actuator. Equation 34 shows that the axial force applied to the structure is independent of the position of the actuator. By extension, A_0 mode selectivity is theoretically independent of the position of the actuator.

To compare to later experiment and simulation, we will determine the theoretical strain induced in an embedded d_{15} and d_{31} PZT for a given electrical field. A d_{31} PZT experiences a tensile strain in the 1 direction as a result of an electric field applied across terminals in the 3 direction. A d_{15} PZT experiences a shear strain in the 1-3 plane as a result of an electric field applied across terminals in the 1 direction (see Figure 10). The strain-charge form of the piezoelectric constitutive equations are as follows [http://www.efunda.com/materials/piezo/piezo_math/math_index.cfm].

$$S = s_E T + d^t E \tag{38}$$

$$D = dT + \varepsilon_T E$$

Here, S denotes the strain, T is the stress, s_E is the compliance, d is the piezoelectric coupling coefficient, and E is the electric field strength. Further, D is the electric charge density displacement, and ε_T is the electric permittivity. The superscript *t* denotes the transpose. In expanded form, the expression for strain is

$$\begin{bmatrix} \varepsilon_{11} \\ \varepsilon_{22} \\ \varepsilon_{33} \\ \gamma_{23} \\ \gamma_{31} \\ \gamma_{12} \end{bmatrix} = \begin{bmatrix} S_{11} & S_{12} & S_{13} & 0 & 0 & 0 \\ S_{12} & S_{22} & S_{23} & 0 & 0 & 0 \\ S_{13} & S_{23} & S_{33} & 0 & 0 & 0 \\ 0 & 0 & 0 & S_{44} & 0 & 0 \\ 0 & 0 & 0 & 0 & S_{55} & 0 \\ 0 & 0 & 0 & 0 & 0 & S_{66} \end{bmatrix} \begin{bmatrix} \sigma_{11} \\ \sigma_{22} \\ \sigma_{33} \\ \tau_{23} \\ \tau_{31} \\ \tau_{12} \end{bmatrix} + \begin{bmatrix} d_{11} & d_{21} & d_{31} \\ d_{12} & d_{22} & d_{32} \\ d_{13} & d_{23} & d_{33} \\ d_{14} & d_{24} & d_{34} \\ d_{15} & d_{25} & d_{35} \\ d_{16} & d_{26} & d_{36} \end{bmatrix} \begin{bmatrix} E_1 \\ E_2 \\ E_3 \end{bmatrix} \tag{39}$$

The d_{15} PZTs used in this study measure 15 mm wide x 15 mm long x 1 mm thick. The d_{31} PZTs in this study are 15 mm wide x 15 mm long x 0.5 mm thick. This difference in thickness was not deliberate and was based solely on the availability of d_{31} PZTs. The d_{15} PZT is embedded in a solid aluminum plate, while the d_{31} PZT is mounted to the surface of the plate (see Figure 11).

In our experiments and simulation, we will not apply any mechanical loading to the PZTs. However, the boundaries of the aluminum and PZTs will be fully bonded, so there will be resulting tensile and shear stress respectively.

We will begin by considering the case of the d_{31} bonded to the surface. An electrical load is applied across the terminals normal to the 3 direction of the PZT. This produces an electric field E_3. The remaining electrical loads, E_1 and E_2 are zero. The only mechanical constraint is in the 1 direction. Thus, σ_{11} is nonzero, while σ_{22} σ_{33} τ_{23} τ_{31} and τ_{12} are zero. The constitutive equation for strain reduces to

$$\varepsilon_{11} = S_{11}\sigma_{11} + d_{31}E_3 \tag{40}$$

When the d_{31} PZT expands, the aluminum will stretch and create a force resisting the strain.

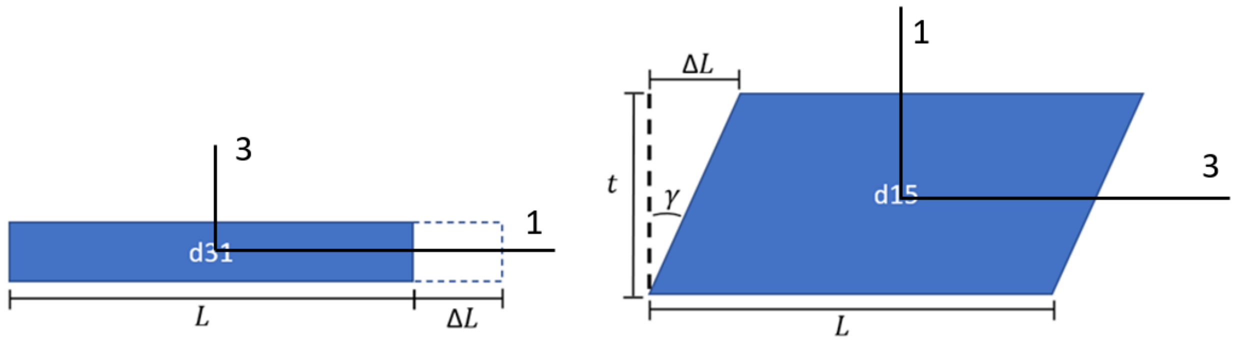

Figure 10: d_{31} and d_{15} free deformation

If we assume no net displacement on the bottom of the d_{15} PZT, we can determine equivalent tensile strain experienced by the d_{15} PZT in terms of the shear strain. The d_{15} PZT experiences a shear strain denoted γ. If the thickness of the d_{15} pzt is *t*, and the effective increase of length of the d_{15} PZT is ΔL, then tan γ is equal to ΔL divided by t. At small angles, tan γ is approximately γ. Thus, it follows that

$$\gamma = \frac{\Delta L}{t} \qquad \text{or} \qquad \Delta L = \gamma t \tag{41}$$

From the definition of normal strain, we have

$$\varepsilon = \frac{\gamma t}{L} \tag{42}$$

From this, we see that the normal strain induced for a given shear strain is inversely proportional to the length-to-thickness ratio. A long, thin d_{15} PZT will produce a smaller normal strain wave than a thick, short d_{15} PZT.

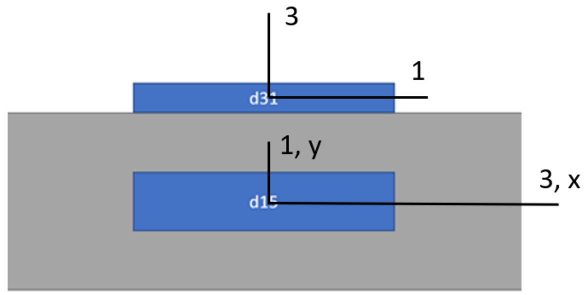

Figure 11: d_{31} and d_{15} PZT in aluminum

4.1.2 Derivation of Analytical Functions for an Embedded Shear Mode PZT

Section 11.4 of Giurgiutiu's Structural Health Monitoring with Piezoelectric Wafer Active Sensors [31] develops theory for selective Lamb wave mode excitation with PZT transducers mounted to the surface of a structure (see Figure *12*a). The Helmholtz equations for pressure and shear wave potentials are solved to find expressions for expected x and y deflection, using the boundary conditions in equation 43.

$$\sigma_{yy}\big|_{y=\pm d} = 0, \quad \sigma_{xy}\big|_{y=+d} = \tau, \quad \sigma_{xy}\big|_{y=-d} = 0 \tag{43}$$

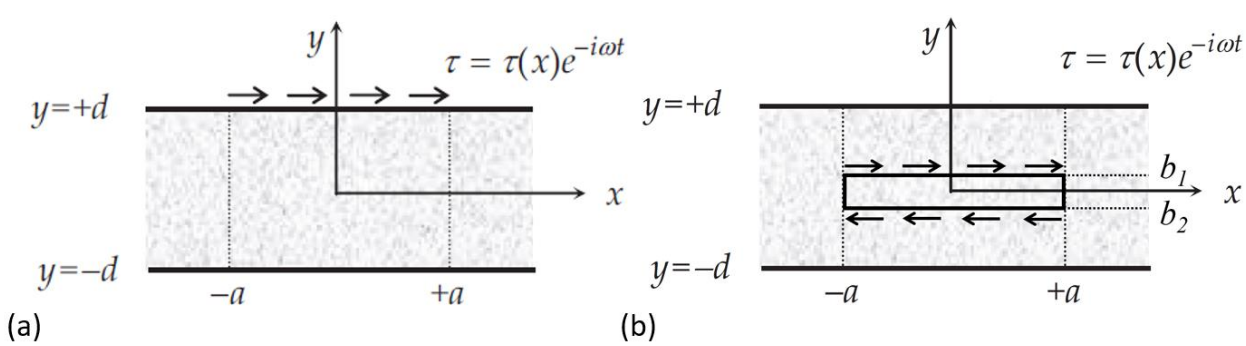

Figure 12: Plate with *PZT* (a) mounted on the surface (b) embedded at the neutral axis. Image adapted from *[31]*.

Giurgiutiu developed expressions for the x component of strain at the surface of the structure as a function of the wavenumber and the tuning functions. In this paper, a similar approach was used to derive expressions for the x and y components of displacement as well as the shear strain in the xy plane and the power flow in the x direction. Figure 12b shows a free body diagram displaying the distributed shear from a shear-mode PZT transducer mounted at the neutral axis of a structure. The transducer has thickness *2b*. If we define *c* as the distance from the neutral axis to the midplane of the PZT, we can express b_1 and b_2 as

$$b_1 = c + b \qquad\qquad b_2 = c - b \tag{44}$$

Again, the Helmholtz equations are solved to find expressions for x and y deflection. This is done by again solving the Helmholtz equations for pressure and shear potentials. Recall that the expressions for shear and normal stress in terms of the pressure and shear potential coefficients are

$$\tau_{yx} = \mu\left[-A_2 2i\xi\eta_p \sin\eta_p y + B_1(\xi^2 - \eta_s^2)\sin\eta_s y + A_1 2i\xi\eta_p \cos\eta_p y + B_2(\xi^2 - \eta_s^2)\cos\eta_s y\right] \tag{45}$$

$$\tau_{yy} = \mu\left[A_2(\xi^2 - \eta_s^2)\cos\eta_p y - B_1 2i\xi\eta_s \cos\eta_s y + A_1(\xi^2 - \eta_s^2)\sin\eta_p y + B_2 2i\xi\eta_s \sin\eta_s y\right]$$

We can now apply a new set of boundary conditions to solve equation 45. Our model consists of a simple beam that is unsupported on either end. Thus, there is zero external load. The boundary conditions used are shown in equation 46. Though the condition of zero normal stress at the top and bottom surfaces of the plate are valid, this boundary condition was not applied. This was to eliminate redundancy and overconstraint in the system of equations.

$$\sigma_{xy}\Big|_{y=\pm d} = 0, \quad \sigma_{xy}\Big|_{y=b_1} = \tau, \quad \sigma_{xy}\Big|_{y=b_2} = \tau \tag{46}$$

Applying the boundary conditions in equation 46 to equation 45 yields the followings system of four equations.

$$2\xi\left(A_1\eta_p\cos\eta_p d - A_2\eta_p\sin\eta_p d\right) + (\xi^2 - \eta_s^2)(B_1\sin\eta_s d + B_2\cos\eta_s d) = 0 \tag{47}$$

$$2\xi\left(A_1\eta_p\cos\eta_p d + A_2\eta_p\sin\eta_p d\right) + (\xi^2 - \eta_s^2)(-B_1\sin\eta_s d + B_2\cos\eta_s d) = 0 \tag{48}$$

$$2\xi\left(A_1\eta_p\cos\eta_p b_1 - A_2\eta_p\sin\eta_p b_1\right) + (\xi^2 - \eta_s^2)(B_1\sin\eta_s b_1 + B_2\cos\eta_s b_1) = \frac{\tau}{i\mu} \tag{49}$$

$$2\xi\left(A_1\eta_p\cos\eta_p b_2 - A_2\eta_p\sin\eta_p b_2\right) + (\xi^2 - \eta_s^2)(B_1\sin\eta_s b_2 + B_2\cos\eta_s b_2) = \frac{\tau}{i\mu} \tag{50}$$

The system of equations was solved symbolically using the commercial software Matlab [33] to find the coefficients A_1, A_2, B_1, and B_2. The coefficients can be expressed as

$$A_1 = -\frac{\tau}{i\mu}\cos d\eta_s \frac{\sin b_1\eta_p \sin d\eta_s - \sin b_1\eta_s \sin d\eta_p - \sin b_2\eta_p \sin d\eta_s + \sin b_2\eta_s \sin d\eta_p}{2\eta_p\xi C} \tag{51}$$

$$A_2 = -\frac{\tau}{i\mu}\sin d\eta_s \frac{\cos b_1\eta_p \cos d\eta_s - \cos b_1\eta_s \cos d\eta_p - \cos b_2\eta_p \cos d\eta_s + \cos b_2\eta_s \cos d\eta_p}{2\eta_p\xi C} \tag{52}$$

$$B_1 = \frac{\tau}{i\mu}\sin d\eta_p \frac{\cos b_1\eta_p \cos d\eta_s - \cos b_1\eta_s \cos d\eta_p - \cos b_2\eta_p \cos d\eta_s + \cos b_2\eta_s \cos d\eta_p}{(\eta_s^2 - \xi^2)C} \tag{53}$$

$$B_2 = -\frac{\tau}{i\mu}\cos d\eta_p \frac{\sin b_1\eta_p \sin d\eta_s - \sin b_1\eta_s \sin d\eta_p - \sin b_2\eta_p \sin d\eta_s + \sin b_2\eta_s \sin d\eta_p}{(\eta_s^2 - \xi^2)C} \tag{54}$$

Where C is defined as

$$\begin{aligned} C = {} & cos\, b_1\eta_p\, cos\, d\eta_s\, sin\, b_2\eta_p\, sin\, d\eta_s - cos\, b_1\eta_p\, cos\, d\eta_s\, sin\, b_2\eta_s\, sin\, d\eta_p - \\ & cos\, b_2\eta_p\, cos\, d\eta_s\, sin\, b_1\eta_p\, sin\, d\eta_s + cos\, b_2\eta_p\, cos\, d\eta_s\, sin\, b_1\eta_s\, sin\, d\eta_p - \\ & cos\, b_1\eta_s\, cos\, d\eta_p\, sin\, b_2\eta_p\, sin\, d\eta_s + cos\, b_1\eta_s\, cos\, d\eta_p\, sin\, b_2\eta_s\, sin\, d\eta_p + \\ & cos\, b_2\eta_s\, cos\, d\eta_p\, sin\, b_1\eta_p\, sin\, d\eta_s - cos\, b_2\eta_s\, cos\, d\eta_p\, sin\, b_1\eta_s\, sin\, d\eta_p \end{aligned} \tag{55}$$

Recall the expression for normal displacement in the x direction from equation 15.

$$u_x = i\xi\left(A_1\sin\eta_p y + A_2\cos\eta_p y\right) + \eta_s(B_1\cos\eta_s y - B_2\sin\eta_s y) \tag{56}$$

If we evaluate at the neutral axis, where y equals zero, the A_1 and B_2 coefficients drop out.

$$u_{x|y=0} = i\xi A_2 + i\eta_s B_1 \tag{57}$$

If we substitute in equation 52 and 53, we get

$$u_x|_{y=0} = i\xi\left(-\frac{\tau}{i\mu}\sin d\eta_s \frac{\cos b_1\eta_p \cos d\eta_s - \cos b_1\eta_s \cos d\eta_p - \cos b_2\eta_p \cos d\eta_s + \cos b_2\eta_s \cos d\eta_p}{2\eta_p\xi C}\right) +$$

$$i\eta_s\left(\frac{\tau}{i\mu}\sin d\eta_p \frac{\cos b_1\eta_p \cos d\eta_s - \cos b_1\eta_s \cos d\eta_p - \cos b_2\eta_p \cos d\eta_s + \cos b_2\eta_s \cos d\eta_p}{(\eta_s^2-\xi^2)C}\right) \tag{58}$$

Equation 58 simplifies to

$$u_x|_{y=0} = \frac{\tau}{\mu}\left(\frac{\xi\left(2\eta_p\eta_s \sin d\eta_p - (\eta_s^2-\xi^2)\sin d\eta_s\right)\left(\cos b_1\eta_p \cos d\eta_s - \cos b_1\eta_s \cos d\eta_p - \cos b_2\eta_p \cos d\eta_s + \cos b_2\eta_s \cos d\eta_p\right)}{2\eta_p\xi(\eta_s^2-\xi^2)C}\right) \tag{59}$$

An expression for the normal displacement in the y direction can be derived similarly. Recall the expression for normal displacement in the y direction from equation 15.

$$u_y = \eta_p\left(A_1 \cos\eta_p y - A_2 \sin\eta_p y\right) - i\xi(B_1 \sin\eta_s y + B_2 \cos\eta_s y) \tag{60}$$

If we evaluate equation 60 at the neutral axis, where y equals zero, the coefficients A_2 and B_1 drop out.

$$u_{y|y=0} = \eta_p A_1 + \xi B_2 \tag{61}$$

If we substitute in equations 51 and 54, we get

$$u_y|_{y=0} = \eta_p\left(-\frac{\tau}{i\mu}\cos d\eta_s \frac{\sin b_1\eta_p \sin d\eta_s - \sin b_1\eta_s \sin d\eta_p - \sin b_2\eta_p \sin d\eta_s + \sin b_2\eta_s \sin d\eta_p}{2\eta_p\xi C}\right) +$$

$$\xi\left(-\frac{\tau}{i\mu}\cos d\eta_p \frac{\sin b_1\eta_p \sin d\eta_s - \sin b_1\eta_s \sin d\eta_p - \sin b_2\eta_p \sin d\eta_s + \sin b_2\eta_s \sin d\eta_p}{(\eta_s^2-\xi^2)C}\right) \tag{62}$$

Equation 62 simplifies to

$$u_y|_{y=0} = \frac{\tau}{\mu}\left(\frac{i\eta_p\left((\eta_s^2-\xi^2)\cos d\eta_s + 2\xi^2 \cos d\eta_p\right)\left(\sin b_1\eta_p \sin d\eta_s - \sin b_1\eta_s \sin d\eta_p - \sin b_2\eta_p \sin d\eta_s + \sin b_2\eta_s \sin d\eta_p\right)}{2\eta_p\xi(\eta_s^2-\xi^2)C}\right) \tag{63}$$

For d_{15} PZTs, shear strain is directly coupled to electric potential. For this reason, we will derive an expression for the shear strain at the neutral axis. We will start by considering Hooke's Law for shear stress and shear strain.

$$\tau_{xy} = \mu\gamma_{xy} \tag{64}$$

Here, γ_{xy} is shear strain in the xy plane, and μ is the shear modulus of elasticity. Recall the expression for shear stress in equation 17.

$$\tau_{xy} = \mu\left[-A_2 2i\xi\eta_p \sin\eta_p y + B_1(\xi^2 - \eta_s^2)\sin\eta_s y + A_1 2i\xi\eta_p \cos\eta_p y + B_2(\xi^2 - \eta_s^2)\cos\eta_s y\right] \tag{65}$$

Solving equation 59 for the shear strain, and substituting in equation 65 yields

$$\gamma_{xy} = \left[-A_2 2i\xi\eta_p \sin\eta_p y + B_1(\xi^2 - \eta_s^2)\sin\eta_s y + A_1 2i\xi\eta_p \cos\eta_p y + B_2(\xi^2 - \eta_s^2)\cos\eta_s y\right] \tag{66}$$

If we evaluate equation 66 at the neutral axis, where y equals zero, the coefficients A_2 and B_1 drop out.

$$\gamma_{xy|y=0} = 2i\xi\eta_p A_1 + (\xi^2 - \eta_s^2)B_2 \tag{67}$$

If we substitute in equations 51 and 54 we get

$$\gamma_{xy}\big|_{y=0} = 2i\xi\eta_p\left(-\frac{\tau}{i\mu}\cos d\eta_s \frac{\sin b_1\eta_p \sin d\eta_s - \sin b_1\eta_s \sin d\eta_p - \sin b_2\eta_p \sin d\eta_s + \sin b_2\eta_s \sin d\eta_p}{2\eta_p\xi C}\right) +$$
$$i(\xi^2 - \eta_s^2)\left(-\frac{\tau}{i\mu}\cos d\eta_p \frac{\sin b_1\eta_p \sin d\eta_s - \sin b_1\eta_s \sin d\eta_p - \sin b_2\eta_p \sin d\eta_s + \sin b_2\eta_s \sin d\eta_p}{(\eta_s^2 - \xi^2)C}\right) \tag{68}$$

Equation 68 simplifies to

$$\gamma_{xy}\big|_{y=0} = \frac{\tau}{\mu}\left(\frac{-2\xi\eta_p(\eta_s^2 - \xi^2)(\cos d\eta_s - \cos d\eta_p)(\sin b_1\eta_p \sin d\eta_s - \sin b_1\eta_s \sin d\eta_p - \sin b_2\eta_p \sin d\eta_s + \sin b_2\eta_s \sin d\eta_p)}{2\eta_p\xi(\eta_s^2 - \xi^2)C}\right) \tag{69}$$

Further analysis can be performed to explore the relationship between neutral axis x and y displacement and shear strain, and the location of the d_{15} PZT actuator. Recall equation 44 from earlier.

$$b_1 = c + b \qquad\qquad b_2 = c - b \tag{70}$$

These equations relate the distance of the PZT top and bottom surfaces from the neutral axis of the structure (b_1 and b_2) to the distance of the PZT midplane to the neutral axis of the structure (c). The terms b_1 and b_2 are found in our expressions of neutral axis x and y displacement and shear strain. We can therefore plot the neutral axis x and y displacement and shear strain as a function of both frequency and PZT distance from the neutral axis c. Plots of these functions are shown in the following figures.

To determine the power flow in the x direction, we must begin by considering the relative power flow density of the A_0 and S_0 modes. Power flow density is defined as the rate of energy transfer per unit area, along the direction of propagation in the structure. It can be thought of as the power transferred through a particular area. The power flow density is equivalent to the product of the velocity vector and the stress tensor. Thus, the power flow density is

$$PFD = -\frac{1}{2}\begin{Bmatrix} \sigma_{11}\left(\frac{du_1}{dt}\right)^* + \sigma_{12}\left(\frac{du_2}{dt}\right)^* + \sigma_{13}\left(\frac{du_3}{dt}\right)^* \\ \sigma_{12}\left(\frac{du_1}{dt}\right)^* + \sigma_{22}\left(\frac{du_2}{dt}\right)^* + \sigma_{23}\left(\frac{du_3}{dt}\right)^* \\ \sigma_{13}\left(\frac{du_1}{dt}\right)^* + \sigma_{23}\left(\frac{du_2}{dt}\right)^* + \sigma_{33}\left(\frac{du_3}{dt}\right)^* \end{Bmatrix} \tag{71}$$

Here, the * symbol denotes the complex conjugate, and the 1 2 and 3 directions correspond to the x y and z directions respectively. In our case, the problem is z invariant, so σ_{xz} and σ_{yz} are zero. Additionally, we are particularly interested in the power flow in the x direction, along the axial direction of the laminate structure. Thus, equation 71 simplifies to

$$PFD_x = -\frac{1}{2}\left(\sigma_{xx}\left(\frac{du_x}{dt}\right)^* + \sigma_{xy}\left(\frac{du_y}{dt}\right)^*\right) \tag{72}$$

To express the power flow density in the x direction, we must first derive an expression for the normal stress in the x direction. We will start with the expression for the normal stress in the x direction from equation 6.

$$\sigma_{xx} = \lambda\left(\frac{d^2\Phi}{dx^2} + \frac{d^2\Phi}{dy^2}\right) + 2\mu\left(\frac{d^2\Phi}{dx^2} + \frac{d^2H_z}{dxdy}\right) \tag{73}$$

We will substitute in the shear and pressure wave potentials, yielding

$$\sigma_{xx} = \left(-\lambda\xi^2 - 2\mu\xi^2 - \eta_p^2\right)\left(A_1 \sin\eta_p y + A_2 \cos\eta_p y\right) + 2\mu\xi\eta_s(B_1 \cos\eta_s y - B_2 \sin\eta_s y) \tag{74}$$

If we evaluate this at the neutral axis where y is zero, the coefficients A_1 and B_2 drop out.

$$\sigma_{xx}|_{y=0} = \left(-\lambda\xi^2 - 2\mu\xi^2 - \eta_p^2\right)A_2 + 2\mu\xi\eta_s B_1 \tag{75}$$

Substituting in equation 62 and 63, we find

$$\sigma_{xx}|_{y=0} = \frac{\tau}{i\mu}\left(\frac{\left(4\mu\eta_p\eta_s\xi^2 \sin d\eta_p - \sin d\eta_s\left(-\lambda\xi^2 - 2\mu\xi^2 - \eta_p^2\right)\left(\eta_s^2 - \xi^2\right)\right)\left(\cos b_1\eta_p \cos d\eta_s - \cos b_1\eta_s \cos d\eta_p - \cos b_2\eta_p \cos d\eta_s + \cos b_2\eta_s \cos d\eta_p\right)}{2\eta_p\xi\left(\eta_s^2 - \xi^2\right)C}\right) \tag{76}$$

Our equations for displacement in x and y are harmonic in time and space. For example, the equation for displacement in the x direction in terms of time and space is

$$u_x(x,t) = u_x e^{i(\xi x - \omega t)} \tag{77}$$

Thus, the derivative of the displacements with respect to time can be expressed as

$$\frac{du_x}{dt} = -i\omega u_x \quad \text{and} \quad \frac{du_y}{dt} = -i\omega u_y \tag{78}$$

We now have all the expressions we need to evaluate the power flow density. However, to determine the power flow, we must integrate the power flow density over the cross-sectional area of the structure. In other words,

$$power\ flow\ in\ x = \int PFD\ dA = \iint PFD\ dy\ dz = t\int_{y=-d}^{y=d} PFD\ dy \tag{79}$$

Here, t is the thickness of the structure in the z direction. Since the problem is z-invariant, t can be moved outside the integral. The integral was solved numerically using Matlab.

4.1.3 Analytical Results for Embedded d_{15} PZT (Displacement, Power Flow)

The expressions derived in the previous section were evaluated for an aluminum plate of 3mm thickness. The expressions were evaluated for frequencies in the range of 0 Hz to 1 MHz, and for distances from the neutral axis to the d_{15} PZT in the range of 0 to 0.99 mm. Note that when the PZT is 1mm from the neutral axis, the 1mm thick PZT is flush with the surface of the aluminum plate. Thus, our model would no longer be valid, and these expressions would be incorrect. The wavenumbers for a given frequency for each the S_0 and A_0 modes were determined using the commercial software Disperse [34].

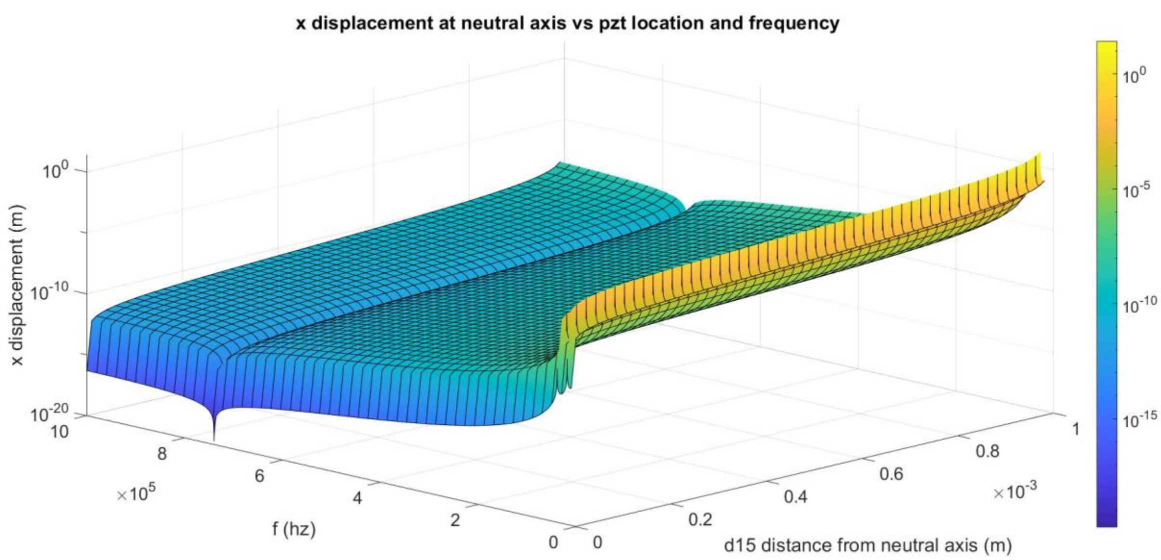

Figure 13: Theoretical x displacement at neutral axis of 3mm thick aluminum plate

The theoretical x displacement at the neutral axis of a 3mm thick aluminum plate is plotted in Figure 13. Note that the displacement at the neutral axis correlates with the S_0 wave amplitude. The x displacement is on the order of 10^{-20} meters when the PZT is at the neutral axis, which is essentially zero. Again, we expect that a d_{15} PZT at the neutral axis will not create S_0 waves. The displacement increases exponentially as the PZT is moved from the neutral axis. For example, at 100 kHz, the displacement is 7 nm for 10 µm, 72 nm for 100 µm, and 505 nm for

500 µm. The displacement decreases at higher frequencies. At 500 kHz, the displacement is 4 pm for 10 µm, 44 pm for 100 µm, and 307 pm for µm. The displacement has a minimum at 739 kHz and maxima at 17.4 kHz and 37.7 kHz. The reasons for these extreme values are not entirely known.

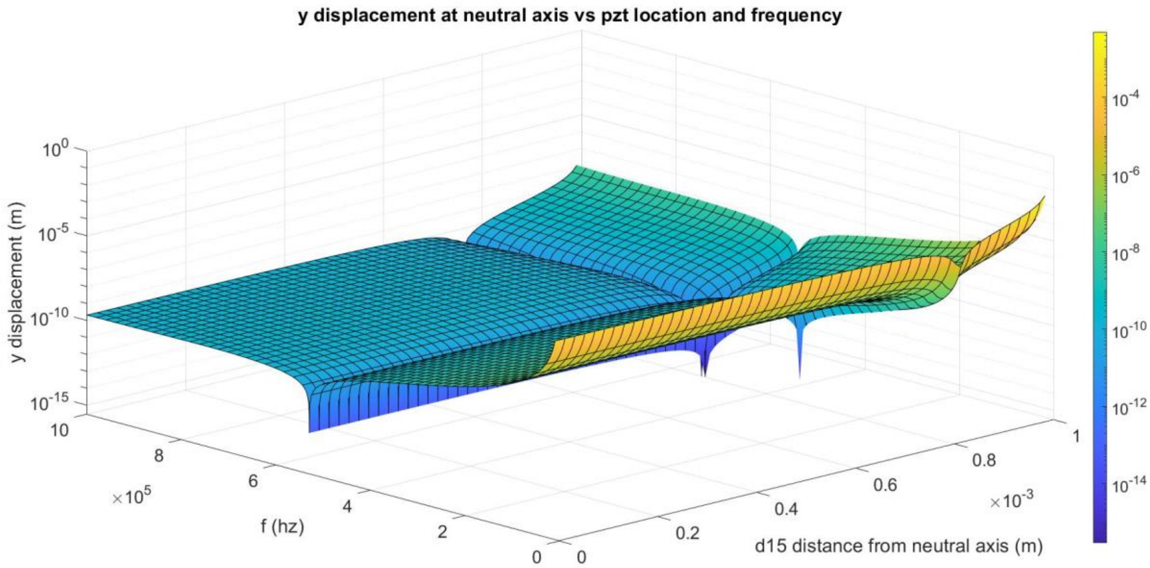

Figure 14: Theoretical y displacement at neutral axis of 3mm thick aluminum plate

The theoretical y displacement at the neutral axis is shown in Figure 14. Unlike the x displacement, the y displacement is non-zero when the PZT is located at the neutral axis. Instead, it is on the order of 10^{-9} meters. The y displacement is initially constant as the PZT is moved off the neutral axis. However, at larger distances, the displacement begins to drop. For example, at 100 kHz, the displacement is 108 nm at 10 µm, 108 nm at 100 µm, and 96 nm at 500 µm. It hits a minimum of 4 nm at 820 µm, before it begins to climb exponentially. At 990 µm, the y displacement is 3.4 µm. The distance from the neutral axis at which the displacement is minimum changes as the frequency increases. The minimum location changes from 820 µm at low frequency to 760 µm at 1 MHz. The nature of this phenomenon is unknown, but it is expected that it is related to the shear strain at the neutral axis, which will be shown later.

The y displacement does seem to increase at low frequency. It is believed that this is a result of the higher energy content of low frequency waves. There is also a minimum displacement at 529 kHz, where the displacement is on the order of 10^{-14} meters, or essentially zero. The nature of this minimum frequency is unknown.

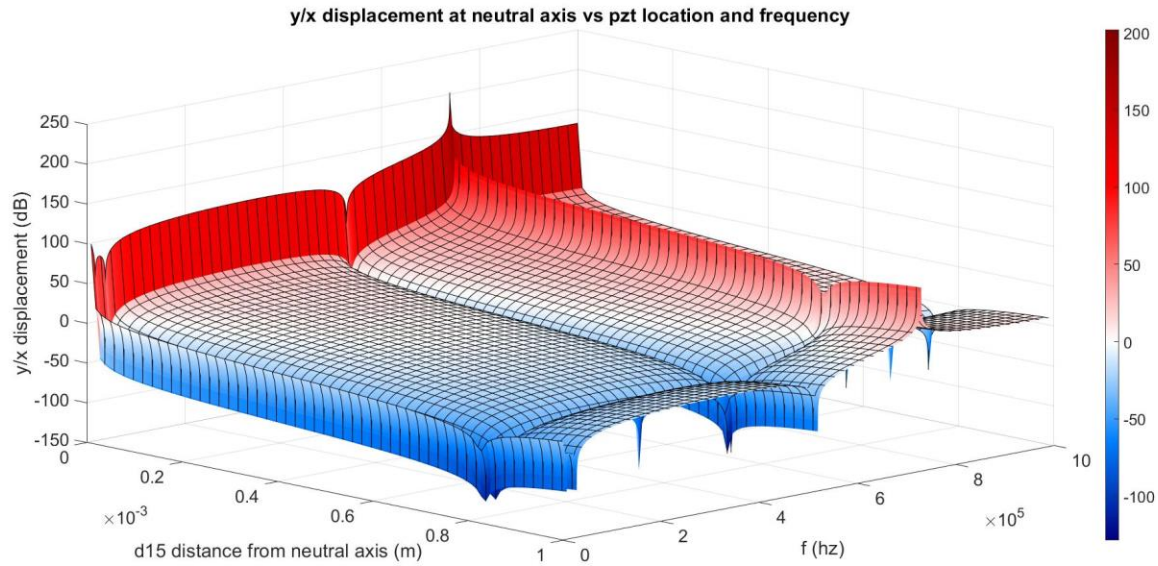

Figure 15: Theoretical y/x displacement ratio in decibels for 3mm thick aluminum plate

The ratio of y displacement to x displacement was calculated and is plotted in terms of decibels, or 20 times the base-ten log of the ratio, in Figure 15. The ratio is very high when the PZT is at the neutral axis. It is approximately 110 dB at low frequency, and 130 dB at higher frequencies. It should be noted that areas of the graph that correspond to 0 dB, or y displacement equal to x displacement, are white in color. Higher frequencies seem to maintain greater y displacement than x displacement for longer, as compared to the lower frequencies. At frequencies from 650 kHz to 1 MHz, the ratio does not reach 0 dB until the PZT is 700 μm from the neutral axis. At frequencies from 300 kHz to 500 kHz, the ratio reaches 0 dB at only 80 μm from the neutral axis. The frequencies of maximum and minimum ratio are results of the frequencies of maximum y displacement and maximum x displacement respectively. The locations that correspond to a minimum y displacement are preserved in this figure.

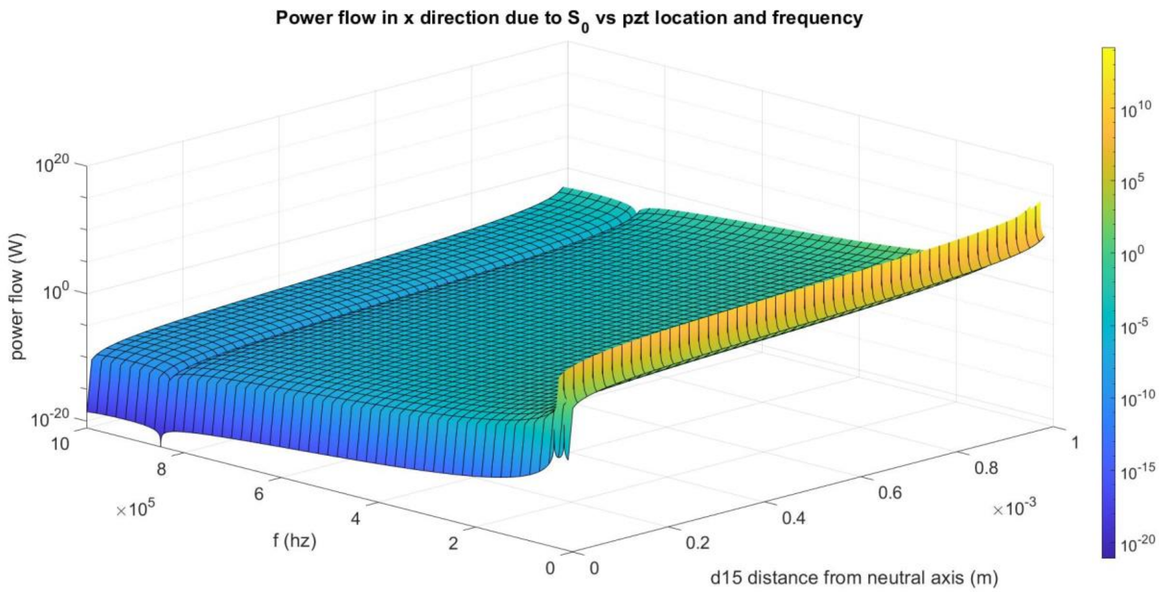

Figure 16: Theoretical power flow due to S_0 in 3mm thick aluminum plate

Because the S_0 and A_0 curves relating frequency and wavenumber are independent, calculating the power flow due to strictly to one mode is trivial. The power flow due to S_0 along the length of the plate is shown in Figure 16. The power flow is essentially zero when the PZT is at the neutral axis. The power flow increases gradually as the PZT is moved off the neutral axis but increases exponentially at further distances. At 100 kHz, the power flow is 800 µW at 10 µm, 820 µW at 100 µm, and 4.04 mW at 500 µm. The power flow decreases at higher frequencies. At 500 kHz, the power flow is 20 nW at 10 µm, 2 µW at 100 µm, and 99 µW at 500 µm. The frequency of minimum power flow is 847 kHz, at which the power flow is on the order of 10^{-11} W. It is not known what causes this minimum, and it does not correspond to the minimum frequency of x displacement.

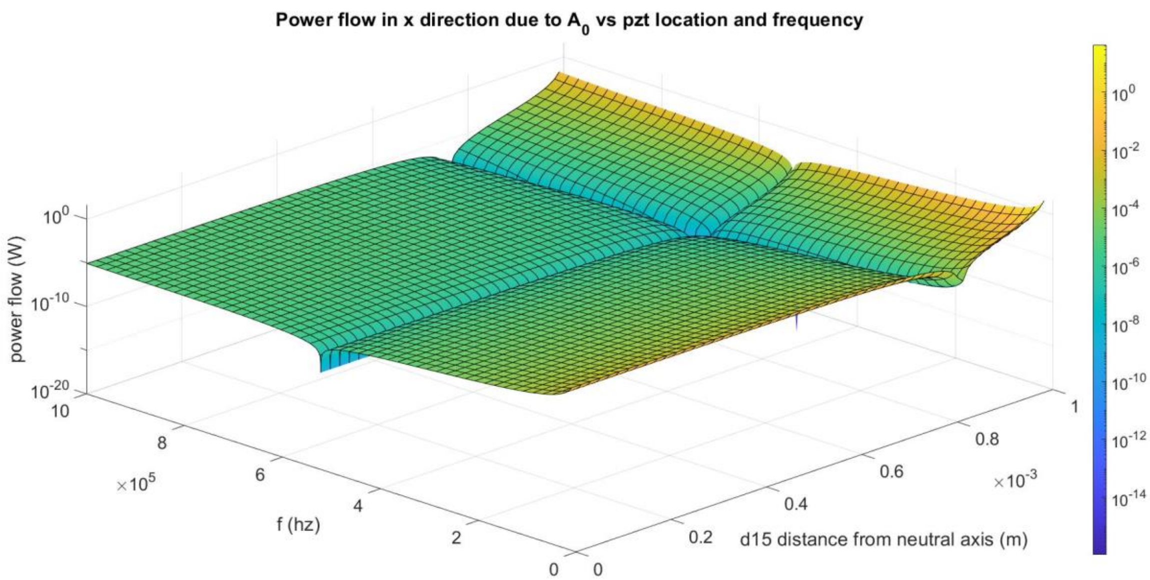

Figure 17: Theoretical power flow due to A_0 in 3mm thick aluminum plate

The power flow due to A_0 is shown in Figure 17. The power flow initially constant as the PZT is moved off the neutral axis, but like the y displacement, it begins to drop at higher distances. At 100 kHz, the power flow is 34 µW at 10 µm, 34 µW at 100 µm, and 29 µW at 500 µm. The power flow hits a minimum of 4.5 µW at 820 µm. It then rises exponentially to 335 mW at 990 µm. Like we saw in the y displacement graph, the location of minimum power flow changes from 820 µm at low frequency to 760 µm at 1 MHz. The power flow also sees a minimum at 522 kHz. The nature of this phenomenon is unknown, as it does not equal the minimum frequency of y displacement.

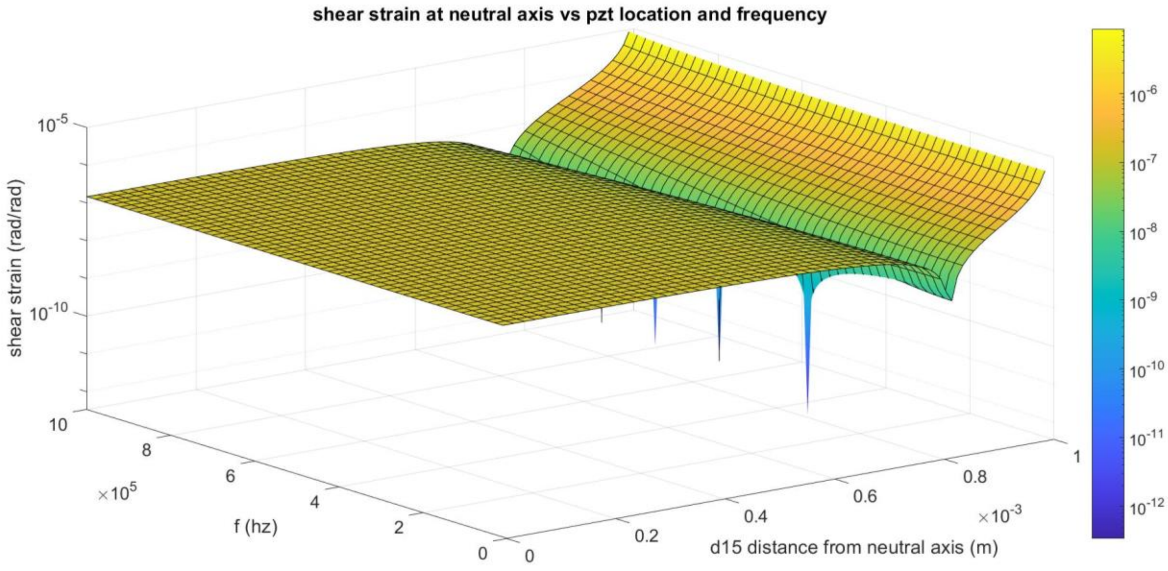

Figure 18: Theoretical shear strain for 3mm thick aluminum plate

The theoretical shear strain at the neutral axis is plotted in Figure 18. It is immediately noticeable that this follows the same pattern we saw in the y displacement. There is a line of minimum shear strain extending from approximately 0.82 microns at 10 kHz, to 0.76 microns at 1 MHz. It is believed that this minimum shear strain is the underlying cause of the minimum y displacement.

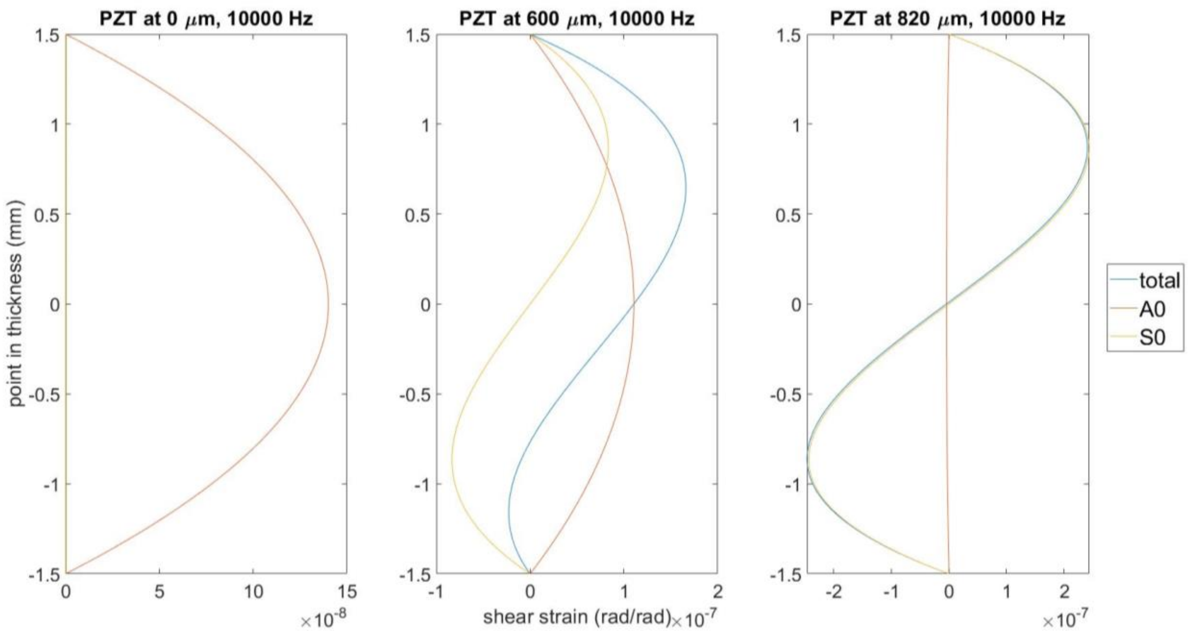

Figure 19: Theoretical through thickness shear strain in 3mm aluminum plate

To determine the cause of this, we will look at plots of the through thickness shear strain (see Figure 19). The shear strain of an S_0 wave is zero at the neutral axis, while the shear strain of an A_0 wave is maximum at the neutral axis. An S_0 wave does not create any shear strain at the neutral axis. While the A_0 and S_0 waves are both present when the PZT is mounted near 760 to 820 µm, it is the superposition of the two waves that causes a minimum at the neutral axis. Thus, it is at these distances that the A_0 wave is at a minimum.

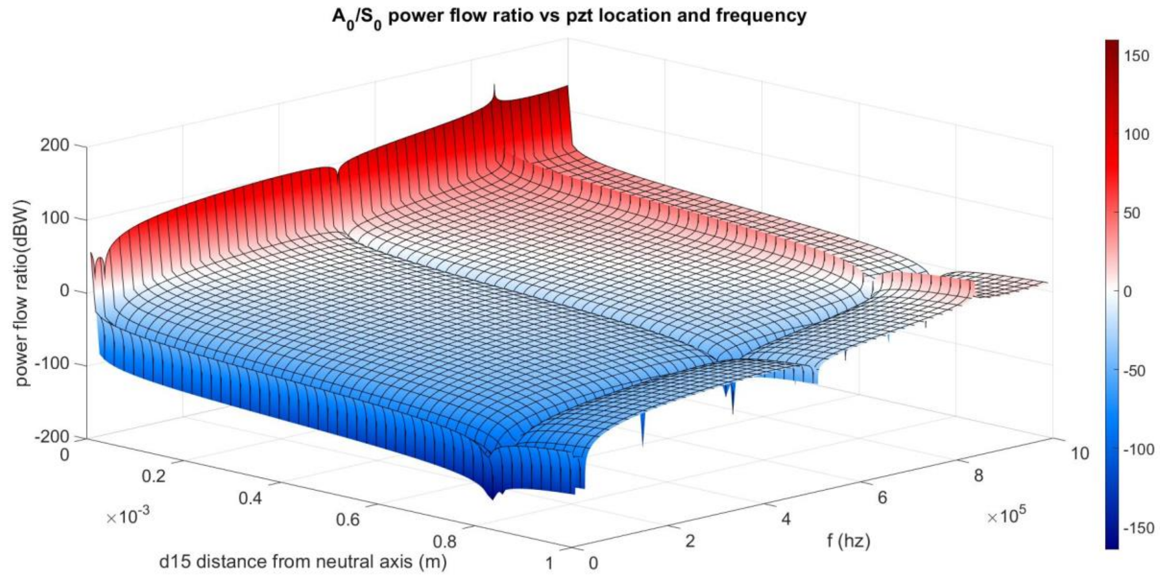

Figure 20: Theoretical A_0 to S_0 power flow ratio for 3mm thick aluminum plate

The A_0 to S_0 power flow ratio is shown in Figure 20. The ratio is reported in decibel Watts, or 10 times the base-ten log of the ratio. The power flow ratio is highest when the PZT is located at the neutral axis. It is approximately 90 dBW or greater at all frequencies. Note that the parts of the graph corresponding to 0 dBW are again colored white.

The PZT must be mounted much closer to the neutral axis to maintain a high power flow ratio, as compared to the y to x displacement ratio. At an actuation frequency of 200 kHz, the PZT must be mounted within 30 µm of the neutral axis to achieve a power flow ratio greater than 0 dBW. At 400 kHz, the allowable distance increases to 100 µm. At 700 kHz, the distance is 460 µm. At 900 kHz, the distance is 690 µm.

Again, we see the line of minimums crossing 0.82 microns at 10 kHz and 0.76 microns at 1 MHz. It is believed that this is caused by the minimum shear strain shown in Figure 18.

4.2 Finite Element Approach

4.2.1 Harmonic Analysis Procedure

A 2D finite element (FE) model was created to analyze the actuation and sensing properties of the d_{15} transducers embedded in the bondline of laminate structures. The piezoelectric properties of the transducers were simulated using multiphysics analyses that couple the electric and mechanical effects simultaneously during the solution process. The FE model was created in ANSYS 19.2. The geometry of the model consisted of an aluminum plate 305 mm x 15 mm x 3 mm in size. The d_{15} PZT actuator and sensor were placed 130 mm apart, with the poling direction aligned along the length of the plate. A d_{31} sensor was placed on the surface of the plate at the location of the d_{15} sensor. A d_{31} actuator was placed on the surface of the plate at the location of the d_{15} actuator. The material properties of the structure components are provided in Table 1.

Table 1: Material properties used in finite element model

Property	Unit	Symbol	PZT-5A	Aluminum
Young's Modulus	10^9 N/m^2	Y_{11}	61.0	68.9
	10^9 N/m^2	Y_{33}	53.2	68.9
Shear's Modulus	10^9 N/m^2	G_{12}	22.6	25.9
	10^9 N/m^2	G_{13}	10.5	25.9
Poisson's ratio	1	ν_{12}	0.35	0.33
	1	ν_{13}	0.44	0.33
Density	kg/m^3	ρ	7600	2700
Dielectric permittivity	8.854 μF/m	ε_{11}	1851	——
	8.854 μF/m	ε_{33}	1581	——
Piezoelectric coefficient	10^{-12} m/V	d_{15}	584	——
	10^{-12} m/V	d_{31}	−171	——
	10^{-12} m/V	d_{33}	374	——

The electromechanical behavior of the d_{15} PZTs was simulated using the coupled field element PLANE223. To accurately simulate wave propagation, it is required to use a mesh size of at least 1/10 of the wavelength [35]. However, a convergence study was performed which indicated that the mesh size should be 0.125 mm. The aluminum was modelled with the structural element PLANE183. A 5-peak Hanning windowed tone burst signal with amplitude of 200V peak-to-peak was applied to the top of the actuator. The bottom of the d_{15} actuator was constrained such that it would have equal voltage at all nodes. The sensing property of the sensor PZTs was achieved in a similar fashion, coupling the voltage at all nodes on the top of the sensor, and coupling voltage at all nodes on the bottom of the sensor. The voltage at the bottom of each sensor was held at 0V, such that the electric potential could be measured by monitoring voltage at the top of each sensor. The interface regions of the structure were modelled as fully bonded joints using contact and target elements. The MPC contact formulation was used to minimize element penetration. Due to the thinness of the modeled structure (15 mm), the plane stress condition was considered.

Early finite element models used a damping ratio of 0.01. Though this produced meaningful results at low frequencies, results achieved for high frequencies were mixed. As frequency increased, voltages at the sensor were reduced, and eventually the waves were completely damped before even reaching the sensor. To remove this inconsistency from the simulation results, damping was eliminated from all models used in this study.

A harmonic analysis of the structure was completed, for the case of a d_{15} actuator and sensor both at the neutral axis. A signal of 100 volts peak-to-peak was applied to the d_{15} actuator. The frequency of the signal was swept from 200 Hz to 1 MHz in 200 Hz increments. The frequency response of shear strain in the d_{15} actuator and sensor was recorded, as well as the voltage produced by the d_{15} sensor. Shear strain in the d_{15} actuator was taken as the average shear strain of all elements in the actuator. The shear strain in the sensor was taken as the average shear strain of all elements in the sensor.

4.2.2 Harmonic Analysis Results (Shear Strain, Voltage Frequency Response)

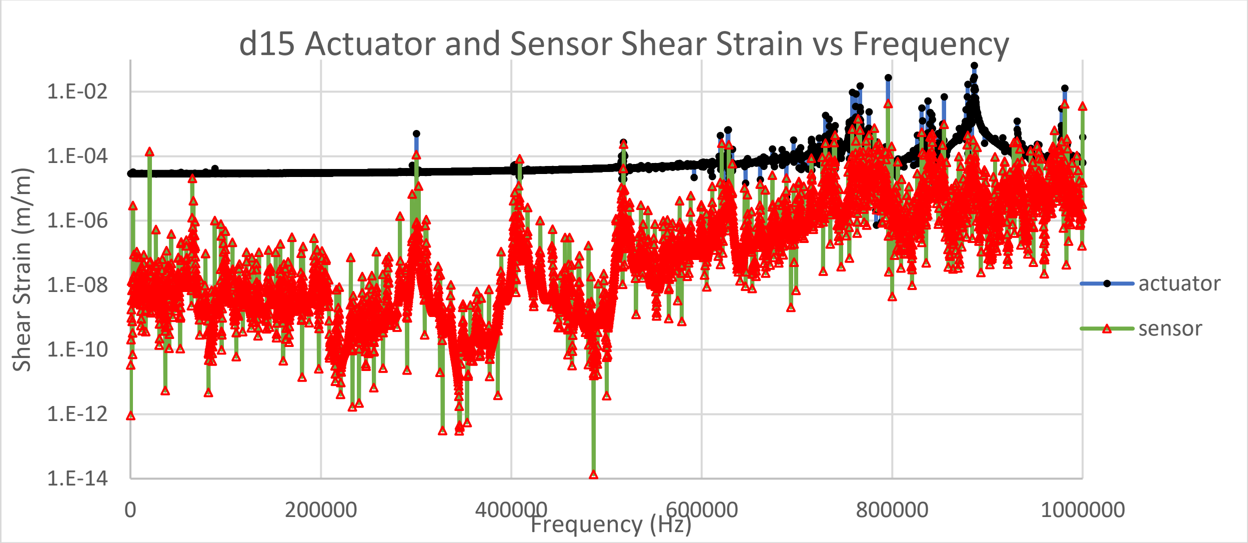

Figure 21: Actuator and sensor average shear strain vs frequency

Because the d_{15} actuator and sensor are shear mode PZTs, the shear strain is inherently coupled to the voltage produced or applied to the PZT. Figure 21 shows the frequency response of the shear strain produced in the d_{15} actuator. It also shows the shear strain induced in the sensor, which is a result of the Lamb waves propagating through the plate. It appears that the actuator has strong natural frequencies at 762 kHz and 886 kHz. These frequencies also produce a strong response in the sensor, though the sensors response at 886 kHz is somewhat attenuated. The actuator also shows several smaller peaks at lower frequencies, for example, at 300, 409, 518, and 628 kHz. These peaks are more obvious in the sensor. Strangely, while the sensor response is greatly attenuated by the structure through most of the frequency spectrum, the response at the natural frequencies is on the same order of magnitude as the actuator.

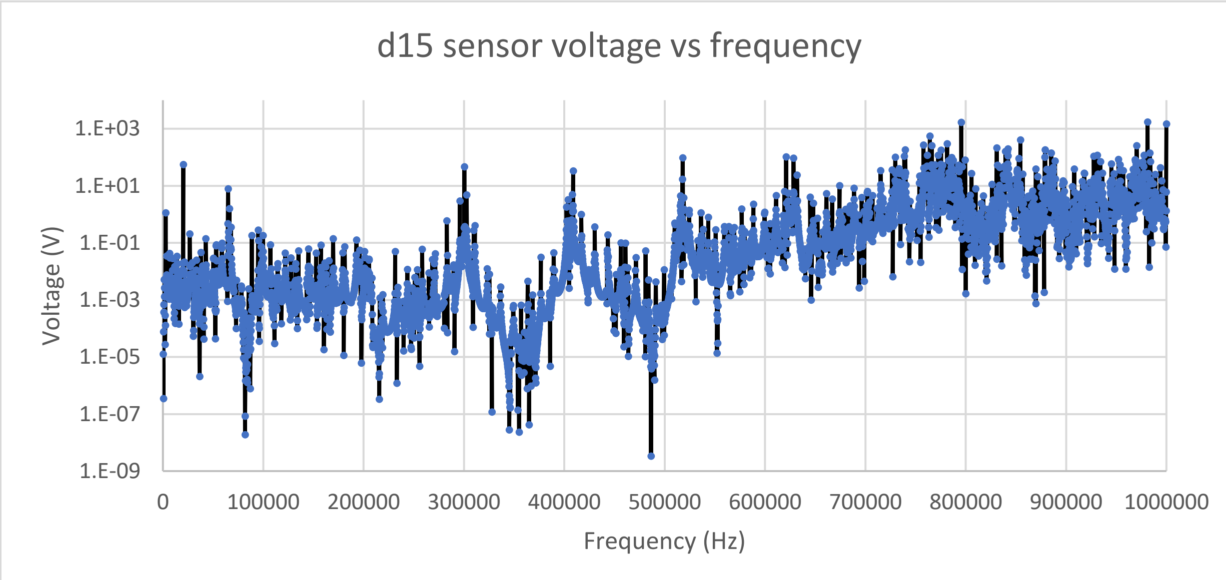

Figure 22: Sensor voltage vs frequency

Figure 22 shows the frequency response of the d_{15} sensor voltage. The natural frequencies, and indeed the entire shape, are consistent with the shear strain shown in figure 5. An important detail to note is the large voltage with respect to the input. The peak at 886 kHz reaches 1700 V, while the input is 100 V. It is expected that this is a result of waves reflecting off the boundaries of the model. Thus, while the relative voltages at each peak are reliable, the absolute voltages are not meaningful. These results are also inconsistent with the experimental results.

4.2.3 Transient Analysis Procedure

Another study was performed to determine the effect of moving the d_{15} actuator off the neutral axis. Vertical position of the d_{15} actuator was varied from 0.001 mm off the neutral axis, to 0.5 mm off the neutral axis. The position of the d_{31} actuator, and the d_{15} and d_{31} sensors were held constant. The maximum x and y displacement induced along nodes on the neutral axis of the beam was recorded.

The neutral axis was monitored between the d_{15} actuator and sensor. Cawley et al. [20] indicate that at the neutral axis, in-plane x displacement can be attributed entirely to the S_0 mode, while out-of-plane y displacement can be attributed entirely to the A_0 mode. By monitoring the maximum x and y displacements along the neutral axis of the beam, the ratio of A_0 to S_0 wave power can be calculated. Early studies indicated that the location of maximum displacement was dependent on the frequency. Additionally, evanescent waves occur in the region nearest the actuator. Thus, the maximum displacement was monitored along the entire region between the actuator and sensor. Figure 23 highlights this region.

Figure 23: Monitored region of neutral axis

This analysis was conducted at several actuation frequencies. To avoid actuation of the A_1 and higher order modes, a maximum frequency-thickness product 1750 kHz-mm should be used. The frequencies explored were 10 kHz, 100 kHz, 200 kHz, 300 kHz, 400 kHz and 500 kHz. The d_{15} and d_{31} sensing voltages were recorded at these frequencies.

An analysis was also conducted using the d_{31} actuator instead of the d_{15} actuator. The frequencies explored were the same as for the d_{15} actuator simulations. The max x and y displacements in the region of interest were recorded, as well as the A_0 and S_0 peak voltages for both the d_{31} and d_{15} sensors.

4.2.4 Transient Analysis Results (Displacement, Shear Strain, Power Flow)

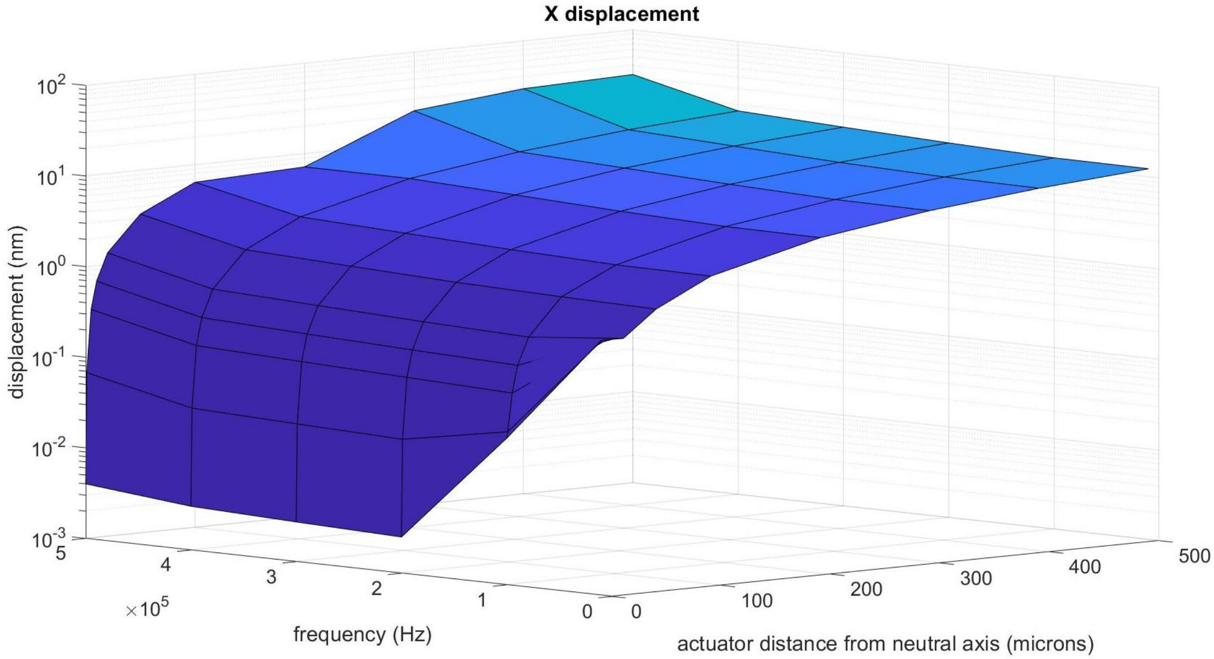

Figure 24: Finite element results for x displacement at neutral axis

X displacement at the neutral axis correlates with the S_0 Lamb wave, while Y displacement at the neutral axis correlates with the A_0 Lamb wave. X displacement at the neutral axis is plotted in Figure 24. As the actuator is moved off the neutral axis, the x displacement scales logarithmically. At 200 kHz, when the PZT is at the neutral axis, the x displacement is only 2.51 pm, which is essentially zero. The x displacement is 143 pm at 5 µm, 1.40 nm at 50 µm, and 14 nm at 500 µm. The displacement somewhat larger for higher frequencies. At 500 kHz, with the PZT at the neutral axis, the x displacement is 4 pm. The displacement is 332 pm at 5 µm, 3.3 nm at 50 µm, and 32 nm at µm. This contrasts with the theoretical x displacement, which decreased as the frequency increased.

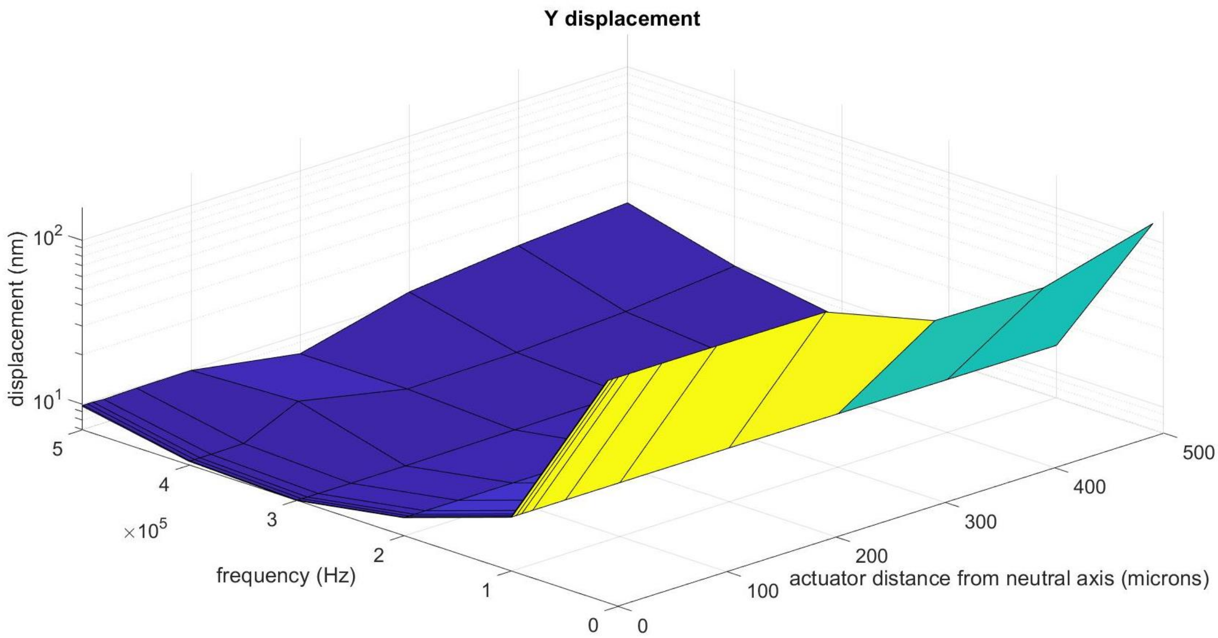

Figure 25: Finite element results for y displacement at neutral axis

Figure 25 shows the y displacement as a function of actuator position and frequency. The y displacement is generally constant with respect to changing the actuator position. At 200 kHz, the displacement is 8.96 nm with the PZT at the neutral axis and 9.08 nm at 500 µm. This is consistent with the theoretical analysis in the previous section. The displacement is largest for an actuation frequency of 10 kHz, and generally decreases with increasing frequency. This trend reflects the convention that low frequency waves have high energy. However, the displacement sees a minimum at 300 kHz, before rising at 400 and 500 kHz. The theoretical displacement saw a minimum at 529 kHz. The simulated displacement is an order of magnitude lower than the theoretical displacement. The simulated displacement at 100 kHz is approximately 14.5 nm, while theoretically it is 108 nm.

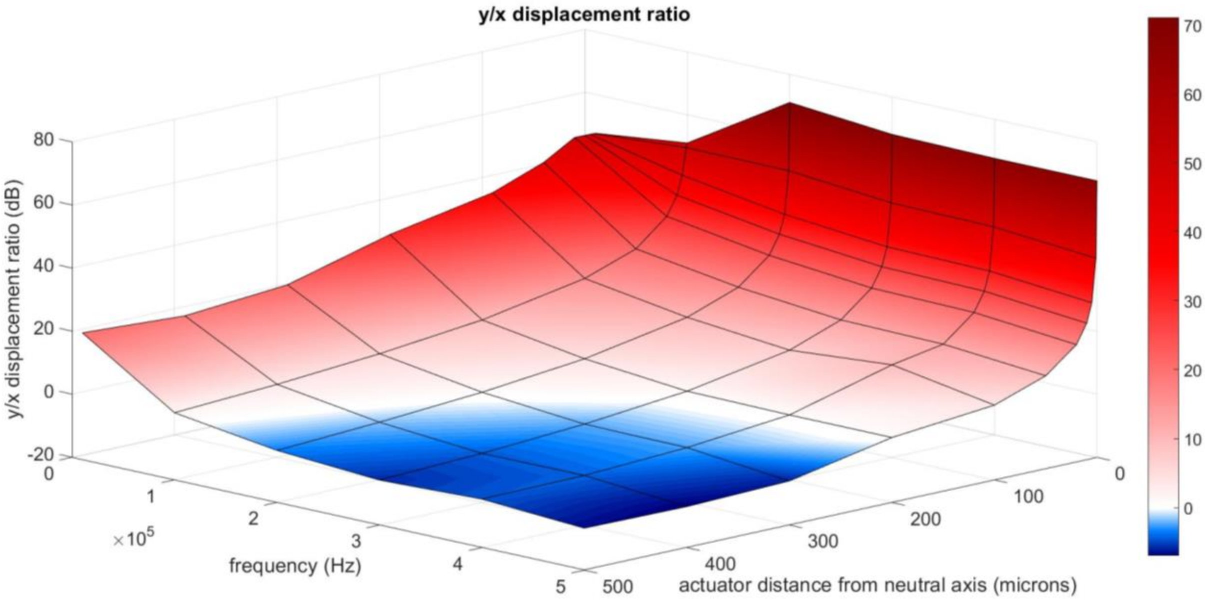

Figure 26: Finite element results for ratio of y to x displacement at neutral axis

The y over x displacement ratio is shown in Figure 26. The ratio is reported as decibels, or 20 times the base-ten log of the y displacement over x displacement. The ratio decreases quickly as the distance from the neutral axis increases. At 200 kHz, the ratio is 71 dB when the PZT is at the neutral axis, and 50 dB when the PZT is 1 micron from the neutral axis. This is consistent with the theory as shown in Figure 15. The simulation ratio also decreases as the frequency increases, unlike the theoretical ratio. This is a result of the flat x displacement with respect to frequency.

The power flow due to the S_0 mode and A_0 mode was calculated using Disperse. Disperse reports the x and y displacements necessary to produce 1 watt of power flow through the structure. Given the necessary x and y displacement at the neutral axis which would produce 1 watt at each frequency, we can calculate the power flow due to each mode. For example, Disperse reports that at 10 kHz an S_0 wave produces an x displacement of 107 nm at the neutral axis, assuming a total of 1 W power flow in the x direction. At the same frequency, Disperse reports that an A_0 wave produces a y displacement of 243 nm, assuming a total of 1 W power flow in the x direction. When our PZT was at the neutral axis and actuated with a 10 kHz toneburst, the simulation reported a max x displacement of 0.65 nm and a max y displacement of 158 nm. Thus, we can calculate that the power flow in x due to S_0 is 0.65/107 W or 6.07 mW, while the power flow in the x direction due to A_0 is 158/243 W or 650 mW. Note that the scaling with respect to 1 W of power flow in Disperse is an arbitrary value, so the absolute power flow due to each mode is incorrect. However, we can rely on this method to correctly represent the relative power flow due to each mode. The power flow is plotted in the following graphs.

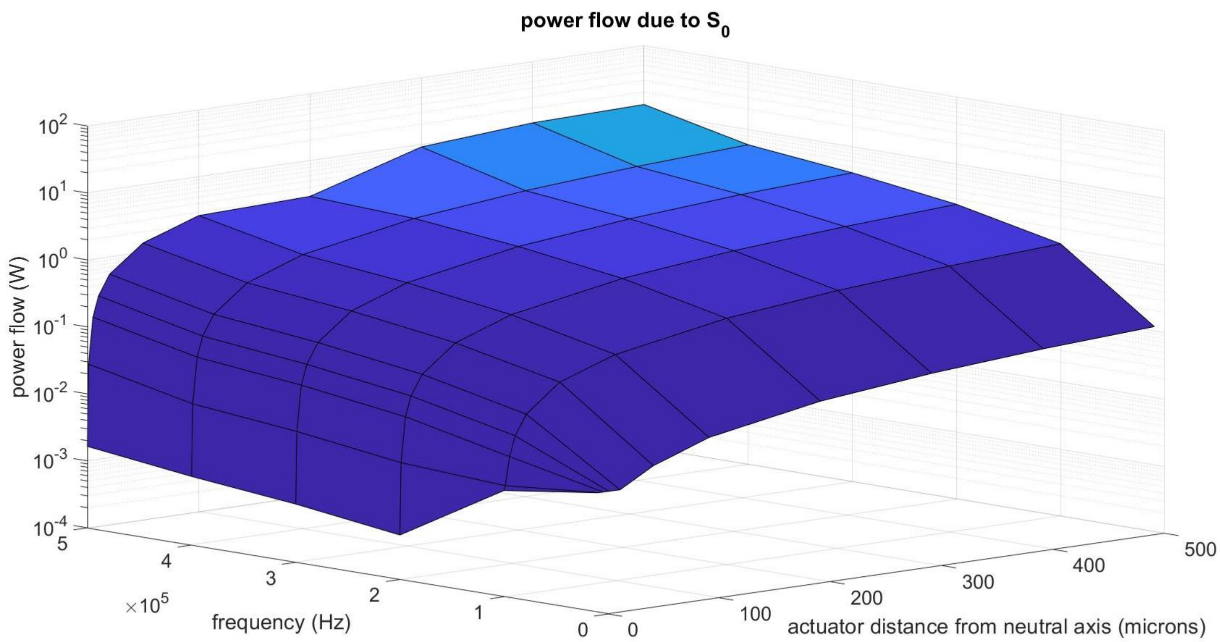

Figure 27: Finite element results for power flow due to S_0

The power flow due to the S_0 mode is shown in Figure 27. The power flow follows the same trend as the x displacement. It increases dramatically as the PZT is moved off the neutral axis, and then it flattens out. Unlike the x displacement, the S_0 power flow is reduced at low frequencies.

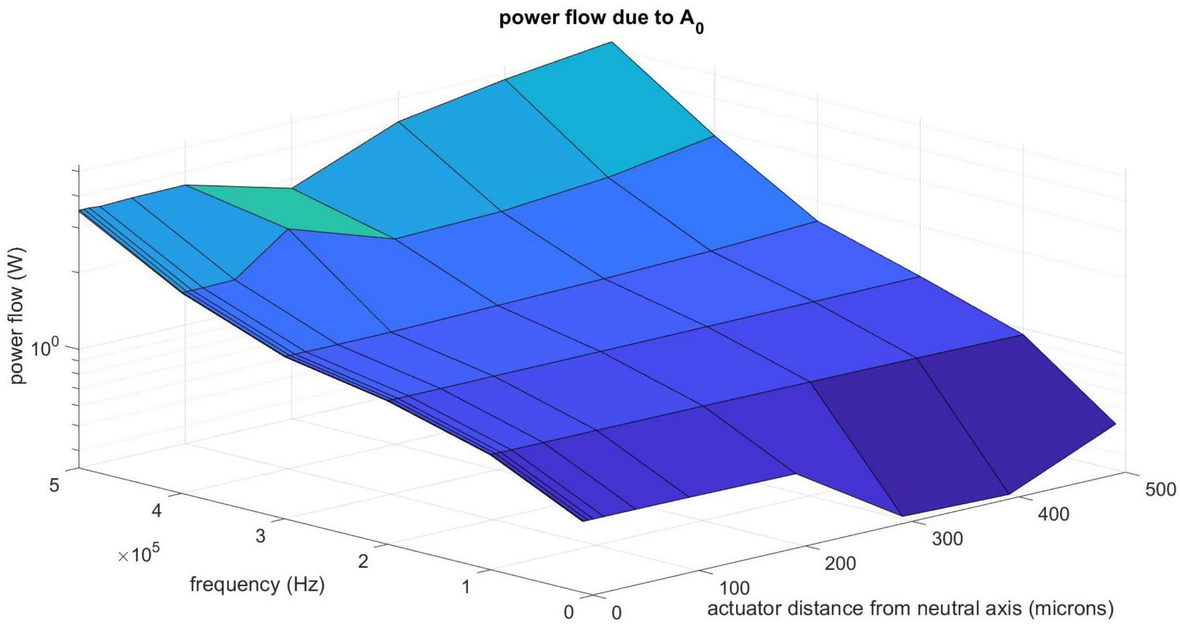

Figure 28: Finite element results for power flow due to A_0

The power flow due to A_0 is shown in Figure 28. The power flow generally stays the same as the PZT is moved off the neutral axis, except for a couple points at 400 and 500 kHz. These variations were carried over from the y displacement. The power flow increases with frequency.

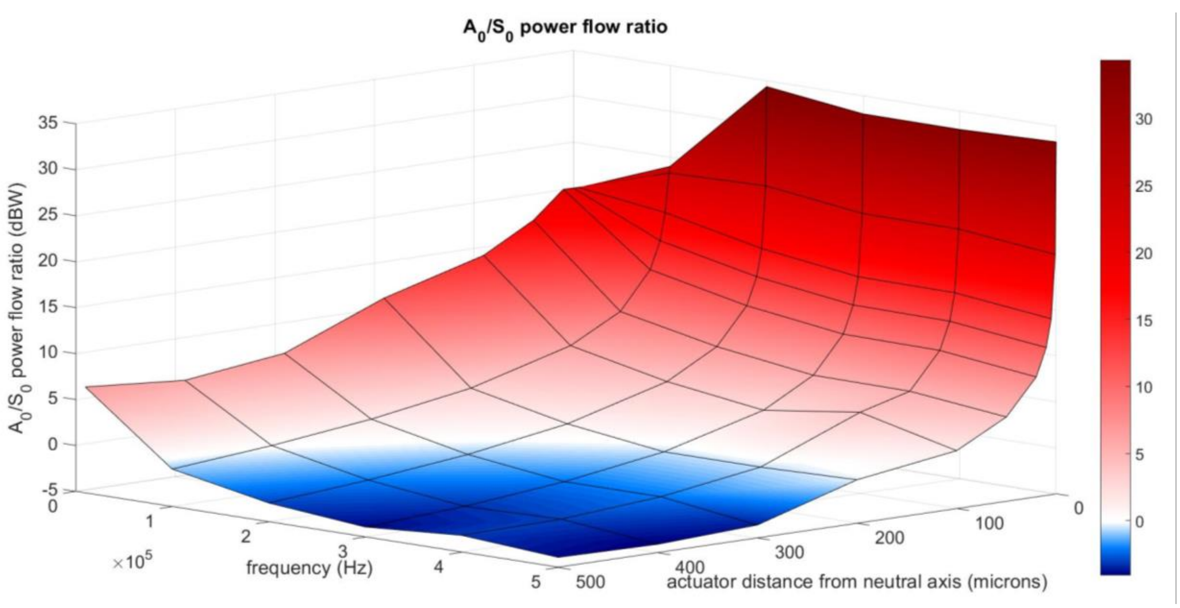

Figure 29: Finite element results for A_0 to S_0 power flow ratio

The A_0 to S_0 power flow ratio is shown in Figure 29. Note that it has the same shape as the graph of y over x displacement in Figure 26. The power flow ratio is highest when the PZT is at the neutral axis and drops quickly as it is moved off axis. The power flow ratio also reduces with increasing frequency. This effect is carried over from the higher y displacement at low frequencies.

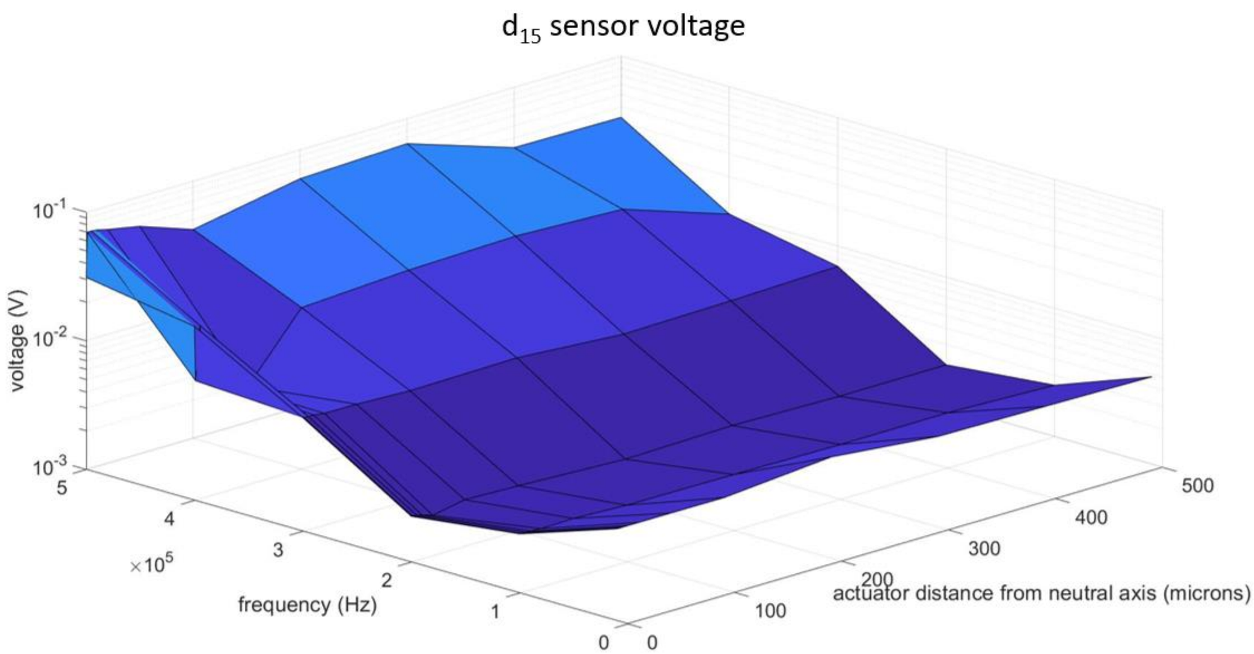

Figure 30: Finite element results for d_{15} sensor voltage vs actuator position and frequency

Figure 30 shows the d_{15} sensor voltage as a function of actuator position and frequency. At low frequency, the d_{15} sensor voltage is generally insensitive to the position of the actuator. This is consistent with theory, as the moment transferred to the structure is constant with respect to the position of the actuator. At 400 and 500 kHz, the voltage decreases somewhat as the actuator is moved off the neutral axis. It is suspected that this behavior is a result of actuating the A_1 mode, which is possible, as we are now actuating in the 1500 kHz-mm range. The voltage hits a minimum at 200 kHz. The cause of this is not clear.

4.2.5 d_{31} Actuation Transient Analysis Results

A simulation was performed in which the d_{31} PZT was actuated instead of the d_{15} actuator. The results are for the case of the d_{15} actuator positioned at the neutral axis, but the effects of d_{15} actuator position are negligible, and should be similar for regardless of the d_{15} actuators position.

Table 2: d_{31} actuator displacements, peak voltages, and A_0 sensing selectivity

frequency (kHz)	x displacement	y displacement	y/x (dBW)	S0 peak voltage d15 (mV)	A0 peak voltage d15 (mV)	S0 peak voltage d31 (mV)	A0 peak voltage d31 (mV)	A0 selectivity d15 (dBV)	A0 selectivity d31 (dBV)
10	9.43E-09	9.62E-07	20.09	20.01	35.20	53.34	92.27	4.91	4.76
100	2.94E-07	2.36E-07	-0.95	6.03	24.54	91.00	651.80	12.20	17.10
200	2.42E-07	2.26E-07	-0.30	1.62	7.86	12.78	176.19	13.71	22.79
300	1.81E-07	2.25E-07	0.95	0.46	6.08	2.69	91.98	22.40	30.67
400	1.81E-07	2.10E-07	0.65	0.46	6.09	2.69	92.03	22.40	30.67
500	1.81E-07	2.10E-07	0.65	0.46	3.58	2.69	39.38	17.77	23.32

Table 2 shows the results for the surface-mounted d_{31} actuator simulations. The y/x displacement ratio is reported in decibel Watts and is calculated as 10 times the base-ten log of the y displacement over the x displacement. The A_0 selectivity is reported as decibel Volts and is calculated as 20 times the base-ten log of the A_0 peak voltage over the S_0 peak voltage. The y-to-x displacement ratio is largest at 10 kHz and is nearly 0 dBW at other frequencies. The d_{31} voltages are noticeably larger than the d_{15} voltages. The A_0 sensing selectivity is on average 6 dBV larger in the d_{31} sensor than the d_{15} sensor. We do not have any theoretical baseline to compare d_{15} and d_{31} selectivity but will later compare this to the result of experiments.

4.3 Experimental Approach

4.3.1 Aluminum Laminate Assembly Procedure

An aluminum laminate specimen was created, to explore determine the A_0 selectivity of each actuator-sensor combination. The test geometry consisted of two d_{15} PZTs sandwiched between two 1-mm thick aluminum sheets, with surface-mounted d_{31} PZTs positioned above the d_{15} PZTs. The aluminum sheets were machined to a size of 305mm x 15mm x 1mm. Then, the shear-mode d_{15} PZTs were adhered to one aluminum sheet using Chemtronics CircuitWorks CW2400 conductive epoxy (Kennesaw, GA, USA) [36]. This sheet would serve as a common ground. The d_{15} PZTs were placed 130 mm apart with their poling direction aligned with the length of the aluminum sheets. The conductive epoxy was then used to attach a 22-gauge wire to the tops of each PZT, which would act as positive terminals. The aluminum sheets were bonded together with a layer of Hysol EA 9394 epoxy (Bay Point, CA, USA) [32]. The epoxy also served as an insulator, preventing shorts between the positive terminals of the PZTs and the top aluminum sheet. The adhesive layer was measured after curing using digital calipers, and it was found to be 1.5 mm. Finally, the CW2400 conductive epoxy was used to mount two d_{31} PZTs to the top of the second aluminum sheet, directly above each of the d_{15} PZTs. Wire was then attached to the top of the d_{31} PZTs, as well as the top of the aluminum sheet, which would act as a second ground. All 4 PZTs were made of APC 850 piezoelectric ceramic material with properties given in [37] [38]

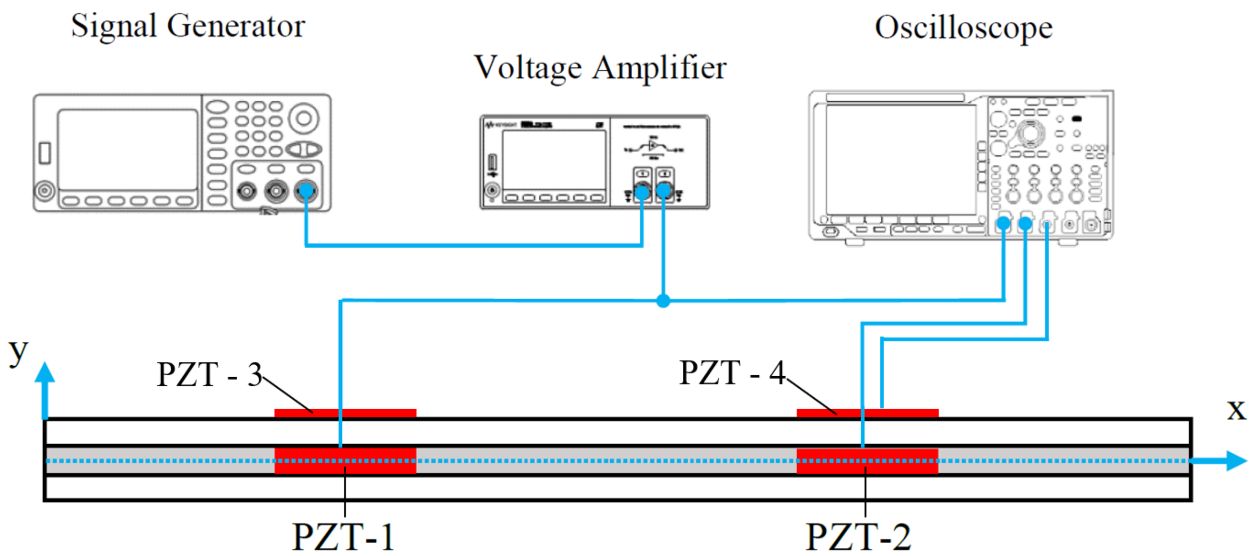

Figure 31: Schematic of experimental setup

The experimental setup to test the specimen is shown in Figure 31. A KEYSIGHT 33500B Series waveform generator [39] was connected to a Krohn-Hite 7602M Wideband Amplifier (Brockton, MA, USA) [40]. In each experiment, the amplifier was connected to either the d_{15} or d_{31} actuating PZT. The actuating PZT and two sensing PZTs were connected to a Tektronix MDO3014 Mixed Domain Oscilloscope [41] to record voltage signals across the actuator and the sensors. The specimen was tested in a pitch-catch configuration by actuating either PZT-1 or PZT-3.

4.3.2 Frequency Response of Aluminum Laminate

Two methods of determining the frequency response were compared, and are discussed in Appendix A. Here, we will use a series of chirp signals and a fast Fourier transform to determine the frequency response of each actuator-sensor combination. A series of experiments was performed using the aluminum laminate sample described in the previous section. First, the series of chirp signals was applied to the d_{15} actuator (PZT-1 in Figure 31). The response was recorded for the d_{15} and d_{31} sensors (PZT-2 and PZT-4). The experiment was repeated, applying the series of chirp signals to the d_{31} actuator (PZT-3). Again, the response was recorded for the d_{15} and d_{31} sensors. To accommodate for the differences in thickness between the d_{15} and d_{31} actuators (1mm and 0.5mm respectively), the voltage applied to the d_{31} PZT was half that applied to the d_{15} PZT. This way, the electric field strength applied to each PZT was equal.

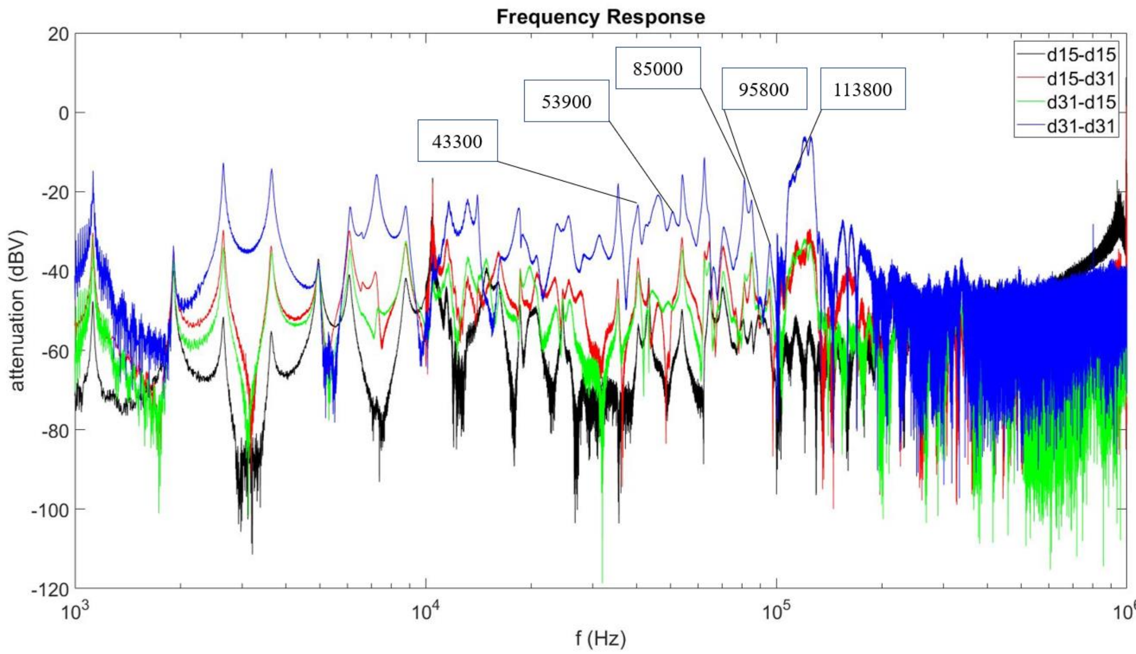

Figure 32: Frequency response for each actuator-sensor pair. Aluminum sample.

The voltage at the d_{31} and d_{15} sensors was recorded for chirp signals applied to the d_{31} and d_{15} actuators. The peak voltages are reported as in voltage decibels, with each voltage normalized by the input voltage. The frequency response is shown in Figure 32. Generally, the strongest response was detected for the case of d_{31} actuation and d_{31} sensing. The weakest response was detected for the case of d_{15} actuation and d_{15} sensing. It should be noted that there is a strong d_{15}-d_{15} and d_{15}-d_{31} response near 900 kHz. This is a result of a resonance frequency of the d_{15} PZT itself. While the d_{15} PZT resonates strongly at this frequency, experiments showed a highly distorted actuation signal when the PZT was stimulated with a toneburst signal. Significant clipping was observed, and the resulting sensor output was heavily distorted. Thus, though the peak to peak voltage is strong at these frequencies, the distorted signals are not suitable for SHM.

4.3.3 Methodology of A_0 Selectivity Analysis

To determine which actuator has stronger A_0 selectivity, we choose a sensor, and compare the output voltages when actuated by the d_{31} PZT to the output voltages when actuated by the d_{15} PZT. To determine which sensor has a stronger A_0 selectivity, we chose an actuator, and compare the output voltages of the d_{31} PZT to the output voltages of the d_{15} PZT.

In total, we have 4 actuator-sensor combinations:

1. neutral-axis d_{15} actuator to neutral-axis d_{15} sensor
2. neutral-axis d_{15} actuator to surface-mounted d_{31} sensor
3. surface-mounted d_{31} actuator to neutral-axis d_{15} sensor
4. surface-mounted d_{31} actuator to surface-mounted d_{31}sensor

To determine the A_0 selectivity, we must determine the ratio of peak A_0 amplitude to peak S_0 amplitude for each actuator-sensor combination. A series of 5-peak Hanning-windowed tonebursts was applied to each of the actuators in turn and the transient response of each sensor was recorded. The toneburst center frequencies were taken at 5 kHz intervals over the range from 5 kHz to 100 kHz.

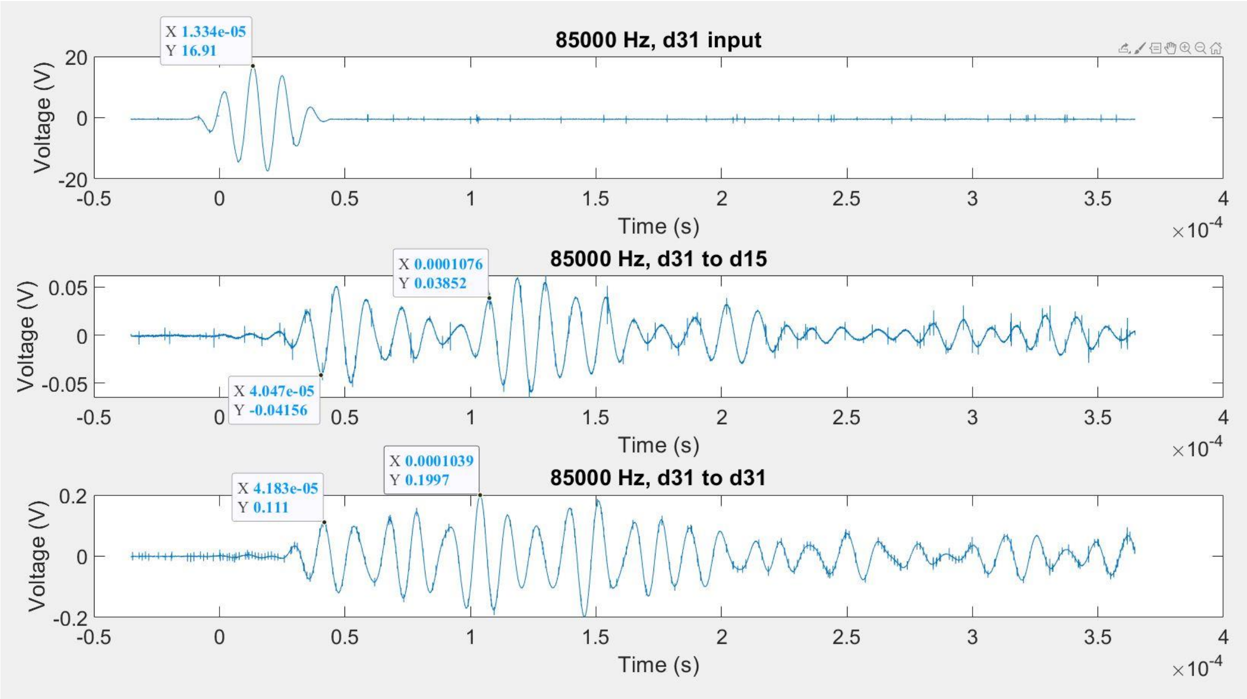

Figure 33: d_{31} actuation response at 85000 Hz. Aluminum sample.

Determination of the exact time and peak voltage of each mode was somewhat subjective due to potential overlap between the S_0 and A_0 signals. The method for determining peaks is illustrated here. Figure 33 shows the response of the d_{15} and d_{31} sensors to a toneburst with a center frequency of 85000 Hz applied to the d_{31} actuator. It also highlights peak voltage input, and the S_0 and A_0 peaks on each sensor.

Determination of the timing of the peaks is aided by examining the group velocity curves. The group velocity of a laminate consisting of two 1mm thick aluminum plates with a 1.5mm epoxy layer was determined using the commercial software Disperse. The group velocity curve is shown in Figure 34. The distance between the actuator and sensors is 130 mm. If we know the group velocity, and the time of the peak input voltage, we can solve for the expected time of arrival of the S_0 and A_0 waves. The initial signal on the d_{15} sensor occurs at the same time as the d_{31} actuator signal. This can be attributed to electromagnetic noise. The remaining signals beyond the A_0 peak are the result of reflections off the end of the structure.

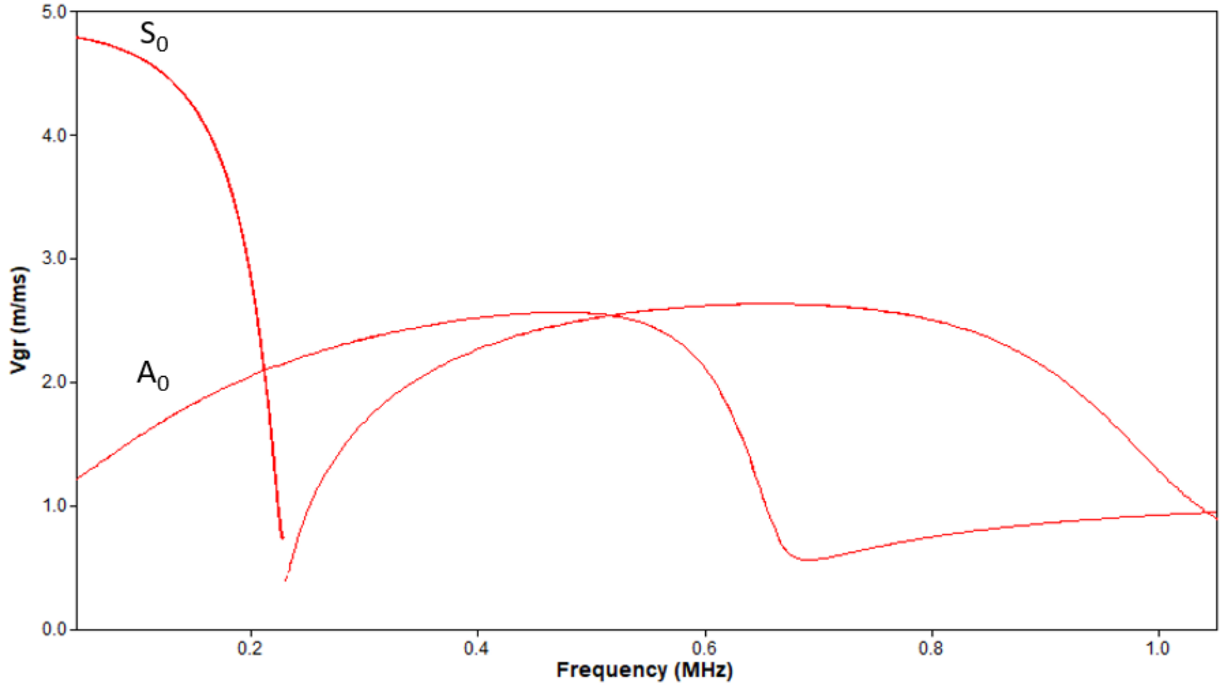

Figure 34: Group velocity curve for aluminum sample

The sensor data was also denoised using a discrete wavelet algorithm in the commercial software Matlab [33]. The function used was "wden". A symlet 8 wavelet was used to decompose the signals. The "minimax" thresholding rule was applied. This rule seeks to minimize the maximum squared error between the original signal and the filtered signal. Hard thresholding and level dependent scaling of the thresholds were used. A six-level decomposition was performed. These settings were determined after a short study by examining the resulting signal after multiple setting changes.

The peak input voltage was found to vary with frequency. Though the applied toneburst is 100 V peak-to-peak, given the finite number of samples, the signal does not technically reach 100 volts. For example, at 45 kHz, the peak input voltage is 92.04 V. The effect is more pronounced at high frequencies. To account for this effect, the output voltages were normalized with respect to the peak input voltages.

This methodology was used to analyze the signals highlighted in Figure 32. Some of the signals were found to be erroneous due to interference between the A_0 peaks and S_0 end reflections. For this reason, the results are reported in Appendix B.

4.3.4 Composite Sample Assembly Procedure

According to theory, as a shear mode PZT is moved off the neutral axis, the S_0 mode actuation should increase, while the A_0 mode actuation should remain the same. To study this experimentally, two carbon fiber composite sandwich structures were created. The intended geometry was similar to the aluminum sample, featuring a 305 mm long carbon fiber composite plate, 15 mm wide and 3 mm thick. Two d_{15} shear mode PZTs were embedded in each sample, while two d_{31} PZTs were mounted to the surface. The experimental setup was the same as that of the aluminum sample (see Figure 31).

To embed the d_{15} PZTs in the carbon fiber, they needed to be electrically isolated. Carbon fiber itself is conductive, so the positive and negative terminals of each PZT must be isolated from one another. First, a 22-gauge wire was attached to each side of a shear-mode d_{15} PZT using Chemtronics CircuitWorks CW2400 conductive epoxy (Kennesaw, GA, USA) [36]. Then, the entire d_{15} PZT was dipped into Hysol 9396 low viscosity epoxy [32]. The PZT was hung by the wires and allowed to cure in an oven. The excess hardened epoxy was trimmed off with a razor to keep the PZT's thickness close to the original 1 mm thickness.

One composite sample had both the actuating and sensing shear mode PZTs mounted at the neutral axis. The second sample had the sensing d_{15} PZT mounted at the neutral axis, but the actuating d_{15} PZT was mounted off the neutral axis. The samples were constructed from Fibre Glast 2214 unidirectional carbon fiber prepreg fabric [42]. This material has a nominal thickness of 152.5 microns. Eighteen strips were cut from the roll of material, each measuring 305 mm long x 15 mm wide. A manual layup was performed using a 3mm thick flat aluminum plate as tooling. First, a sheet of Teflon release material was taped to the plate, using conventional Scotch tape. Then one strip was pressed onto the release material. Five more layers were laid one on top of the other. The carbon fiber strips for the following six layers were cut to allow room for the shear mode PZTs. These strips were laid on top of the six-sheet bottom layer, and the insulated shear mode PZTs were placed in the resulting gaps. Six more layers of the carbon fiber prepreg were laid on top of this. Another layer of Teflon release material was laid on top. Then a layer of absorbent material, which was intended to soak up excess epoxy, was laid on top of the Teflon. The entire assembly, including the aluminum plate, was placed in a vacuum bag and vacuum sealed using a conventional kitchen sealer. The sealed assembly was placed in an oven to cure. The oven was ramped slowly at a rate less than 5^{o} F per minute to a temperature of 310^{o} F. This temperature was held for 1 hour. Then, the oven was turned off, and the sample was allowed to cool slowly to room temperature in the oven.

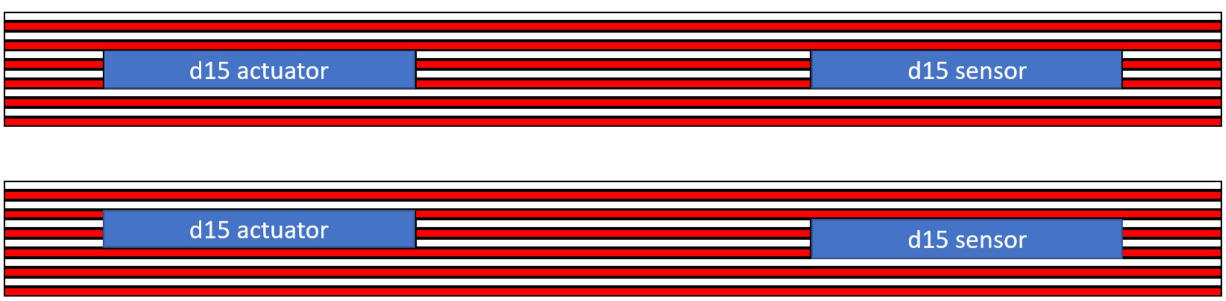

Figure 35: (Top) both d_{15} PZTs at neutral axis (bottom) actuator off axis. Not to scale. Color added for contrast.

An identical procedure was used to construct the second sample. However, the carbon fiber sheets were arranged strategically to place the actuating PZT off the neutral axis. Six layers formed the bottom of the sample. The sensing PZT was placed on top of the 6th layer, and the 7th layer was cut and placed around the PZT. The actuating PZT was placed on top of the 7th layer.

In this way, the actuating PZT would be mounted off the neutral axis by 1 layer's thickness, or 152.4 microns nominally (see Figure 35). Each sample's final dimensions were measured, and they were found to be 4.5mm thick, while the nominal thickness of the prepreg sheet suggested a final thickness of approximately 3mm. This implies that the final dimension of each layer was 250 microns, or 0.25 mm. Thus, the actuating PZT was mounted off axis by a distance equal to 5.5% of the sample's thickness.

4.3.5 d_{15} Actuation Selectivity vs Distance from Neutral Axis

A series of 5 peak Hanning-windowed tonebursts was applied to the d_{15} actuators of each composite sample. The range of frequencies explored was 5 kHz to 100 kHz. Data was recorded at 5 kHz intervals. These low frequencies were used because the speeds of the A_0 and S_0 modes and arrival times are more different than at high frequency. The peak voltages were determined using the methodology described in the section 4.3.3.

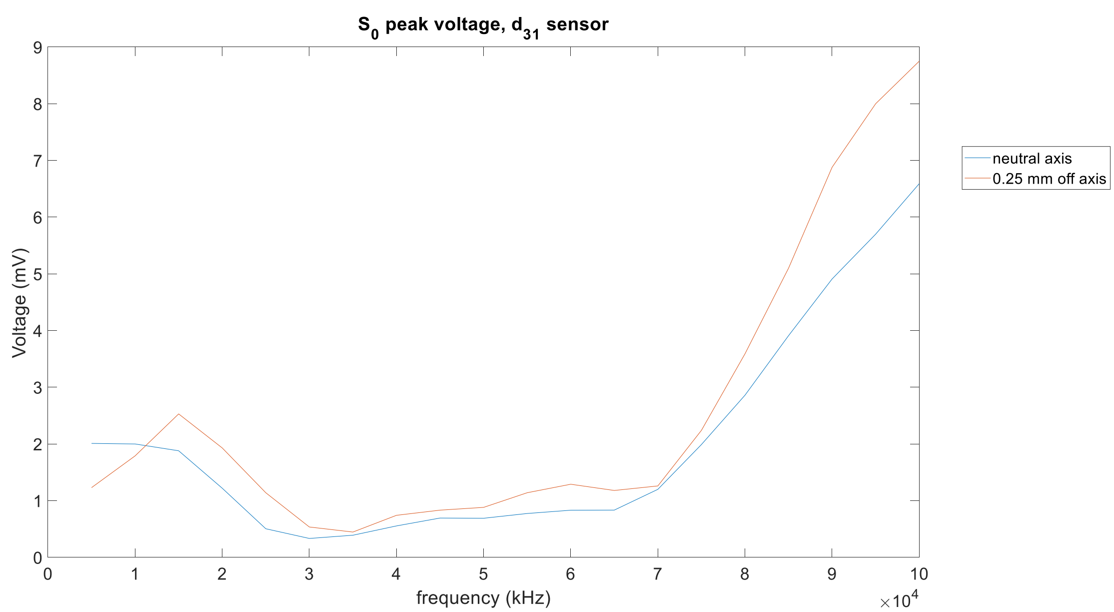

Figure 36: Peak S_0 wave voltage vs frequency for each composite sample. d_{15} actuator, d_{31} sensor.

Figure 36 shows the peak S_0 wave voltage for the two composite samples. The peak voltage increases as the actuator is moved off the neutral axis for all frequencies. This is consistent with theory and simulation.

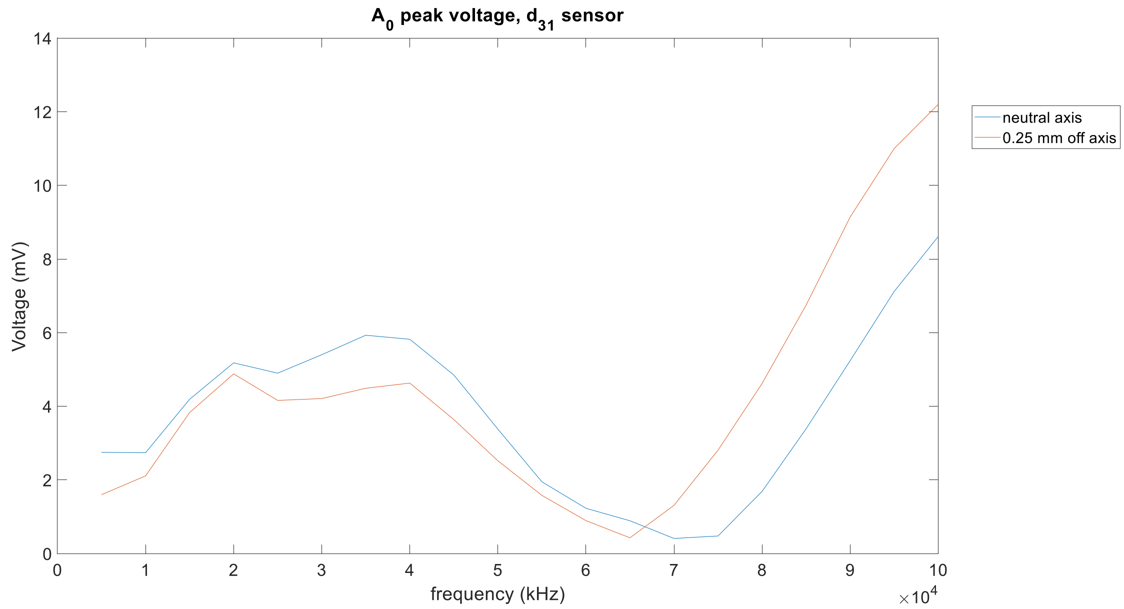

Figure 37: Peak A_0 wave voltage vs frequency for each composite sample. d_{15} actuator, d_{31} sensor.

The peak A_0 wave voltage for the two composite samples is shown in Figure 37. At frequencies below 70 kHz, the voltage decreases when the PZT is moved off the neutral axis. At 70 kHz and higher, the voltage increases. The relationship between the wavelength of the A_0 wave and the distance between the d_{15} actuator and d_{31} sensor was considered. At 35 kHz, the A_0 wavelength is 33 mm. At 100 kHz, the A_0 wavelength is 14 mm. At 68 kHz, the wavelength is approximately 20 mm, while the distance measures 130 mm. The distance is 6.5 times the wavelength at this frequency. However, many integer multiples of the wavelengths between 14 and 33 mm exist which are equal to 130 mm. Since only 1 minimum is found in our data, it is unlikely that this relationship is the primary cause.

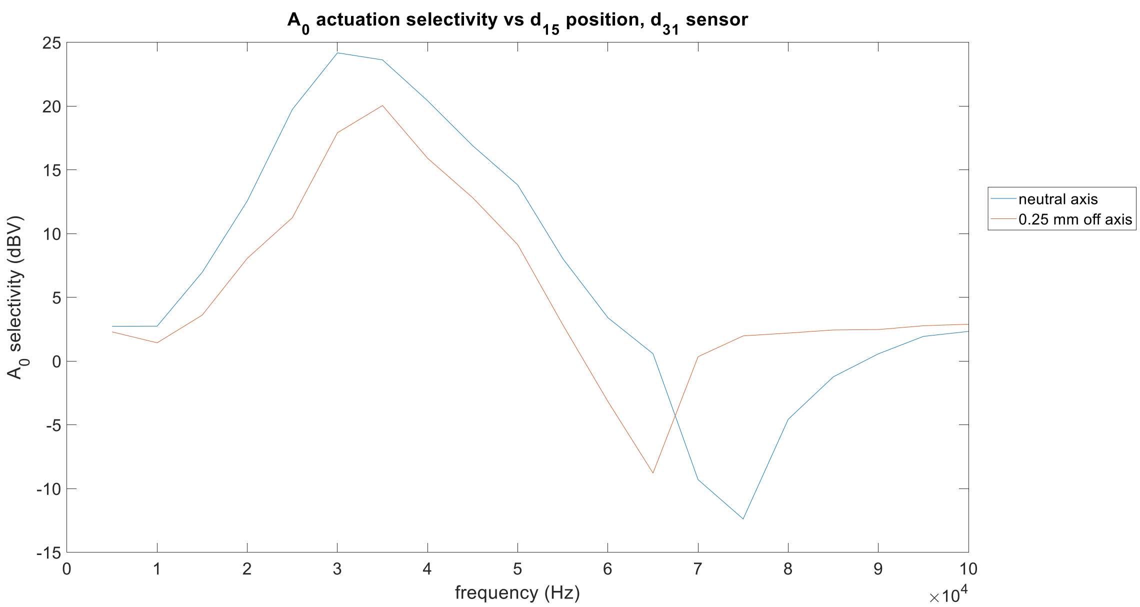

Figure 38: A_0 mode actuation selectivity as d_{15} PZT is moved off axis. Composite samples. d_{15} actuator, d_{31} sensor.

The A_0 selectivity is defined here as the ratio of the peak A_0 voltage to the peak S_0 voltage. It is reported in dBV and calculated as 20 times the base-ten log of the ratio. The average actuation selectivity when the d_{15} actuator is located at the neutral axis is 12.7 dBV. The average actuation selectivity when the d_{15} actuator is located 0.25 mm off the neutral axis, or 5.5% of the sample's thickness, is 8.68 dBV, a drop of 4.02 dBV. This is equivalent to a drop of 0.73 dBV per % of the sample's thickness that the PZT is moved off axis.

4.3.6 d_{15} vs d_{31} Actuation Selectivity

We have now confirmed that the A_0 actuation selectivity of the d_{15} PZT is maximized when it is at the neutral axis, but we do not know how this selectivity compares to measurements made with conventional surface-mounted d_{31} PZTs. To compare the A_0 actuation selectivity of the d_{15} and d_{31} PZTs, we must compare the signals of the d_{15} and d_{31} actuators when sensed by a common sensor. Thus, we could compare d_{31}-to-d_{31} with d_{15}-to-d_{31}, and d_{31}-to-d_{15} with d_{15}-to-d_{15}. Both comparisons will allow us to determine d_{15} and d_{31} actuation selectivity, and the difference in actuation selectivity should be independent of which sensor's data we use. However, it is expected that there will be larger values of selectivity in the signals sensed with the d_{15} PZT.

At this point in the study, access to the lab was limited. However, earlier experiments provided enough data to calculate the A_0 selectivity of a d_{31}-to-d_{31} configuration, as well as the d_{31}-to-d_{15} configuration. Note that sampling of the frequency spectrum was not ideal for the comparison.

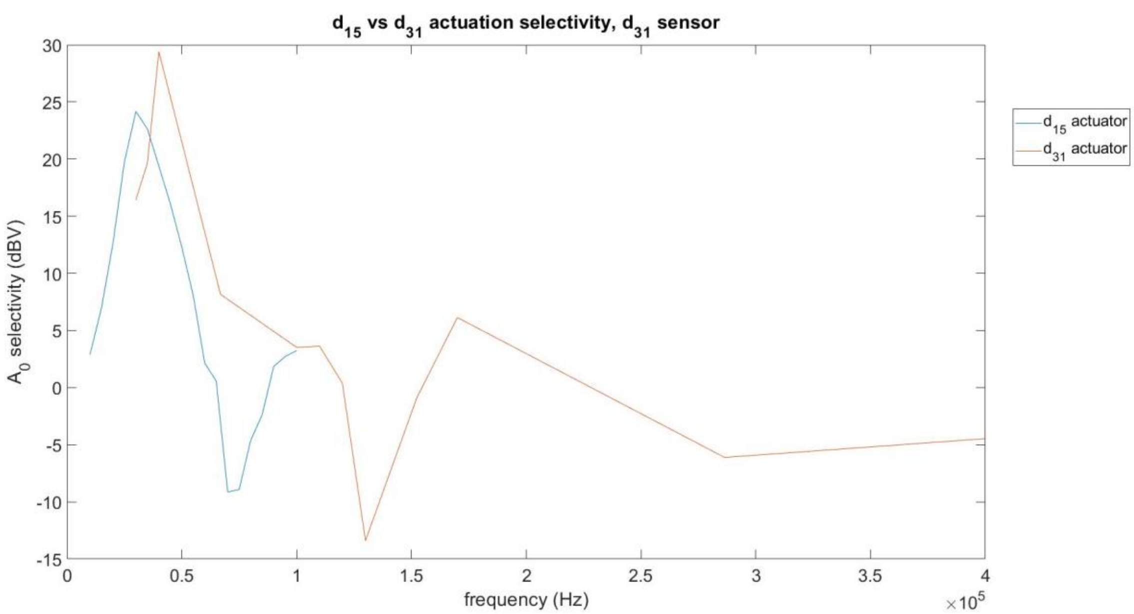

Figure 39: A_0 actuation selectivity of d_{15} and d_{31} PZT measured with d_{31} sensor. Composite sample.

The d_{15} and d_{31} actuation selectivity is shown in Figure 39. This figure shows selectivity determined by comparing signals measured with a d_{31} sensor. Though we do not have a full picture of the selectivity for each configuration at each frequency, we can still draw some conclusions from the data. The average A_0 selectivity is calculated as 20 times the base-ten log of the average ratio of A_0 to S_0 voltage. The average ratio is determined by numerically integrating the ratio at all frequencies and dividing by the frequency range. The average A_0 selectivity for the d_{15}-to-d_{31} configuration and d_{31}-to-d_{31} configuration are 12.7 dBV and 7.89

dBV respectively. The d_{15} actuator shows an average of 4.81 dBV higher A_0 selectivity when measured with a surface-mounted d_{31} sensor.

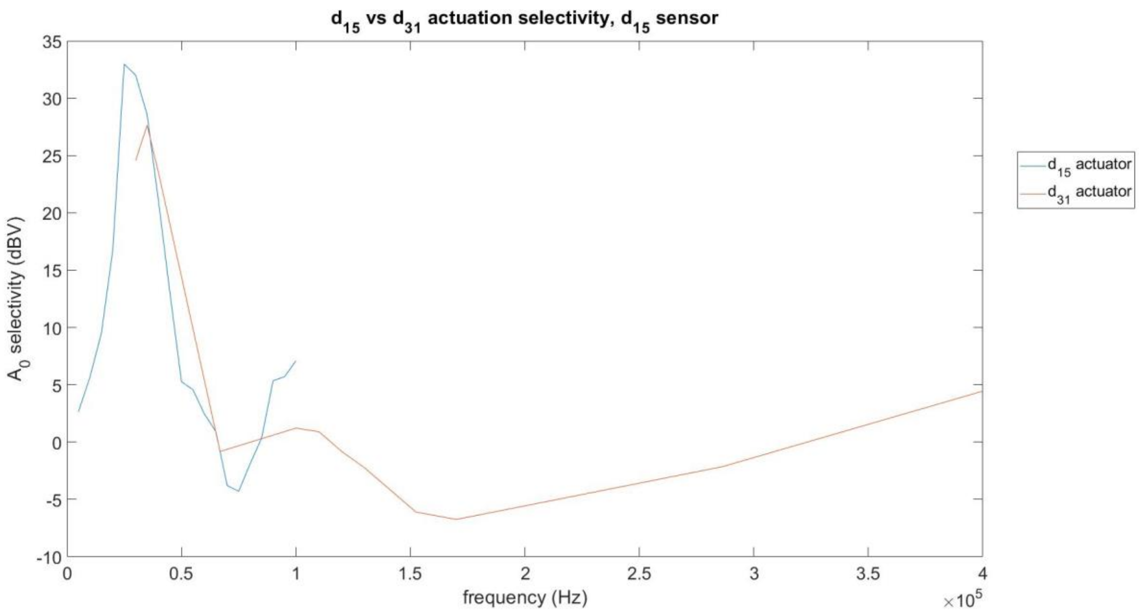

Figure 40: A_0 actuation selectivity of d15 and d31 PZT measured with d_{15} sensor. Composite sample

The analysis was repeated using signals measured with a d_{15} sensor. The average A_0 selectivity for the d_{15}-to-d_{15} configuration and d_{31}-to-d_{15} configuration are 18.1 dBV and 5.67 dBV respectively. The d_{15} actuator shows an average of 12.43 dBV higher A_0 selectivity when measured with a neutral axis d_{15} sensor.

Table 3: A_0 actuation selectivity

	d_{15} actuation selectivity (dBV)	d_{31} actuation selectivity (dBV)	d_{15} advantage (dBV)
sensed with d_{31}	12.7	7.89	4.81
sensed with d_{15}	18.1	5.67	12.43

Table 3 summarizes the reported A_0 actuation selectivity of each PZT. The d_{15} PZT is a more selective actuator, regardless of which sensor is used.

4.3.7 d_{15} vs d_{31} Sensing Selectivity

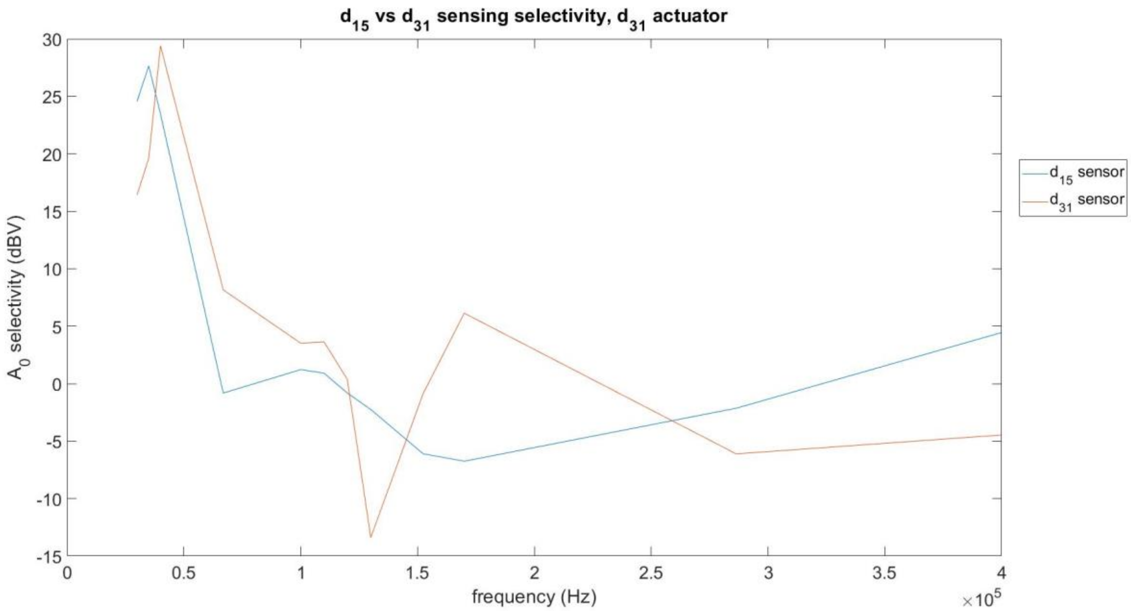

Figure 41: A_0 sensing selectivity of d_{15} and d_{31} PZT stimulated with d_{31} actuator. Composite sample.

To compare the A_0 sensing selectivity of the d_{15} and d_{31} PZTs, we must compare the signals of the d_{15} and d_{31} sensors when actuated by a common actuator. Thus, we could compare d_{31}-to-d_{31} with d_{31}-to-d_{15}, and d_{15}-to-d_{31} with d_{15}-to-d_{15}. The A_0 selectivity of each sensor was compared, using the composite sample with both d_{15} PZTs positioned at the neutral axis. The d_{15} PZT was actuated and the output voltages of each the d_{15} and d_{31} sensors were compared. The PZT was actuated at frequencies of 10 kHz to 100 kHz, at 5 kHz intervals. Figure 41 shows the A_0 selectivity for each sensor. The average A_0 selectivity for the d_{31}-to-d_{15} configuration and d_{31}-to-d_{31} configuration are 5.67 dBV and 7.89 dBV respectively. The d_{31} sensor shows an average of 2.22 dBV higher A_0 selectivity when stimulated with a surface-mounted d_{31} actuator.

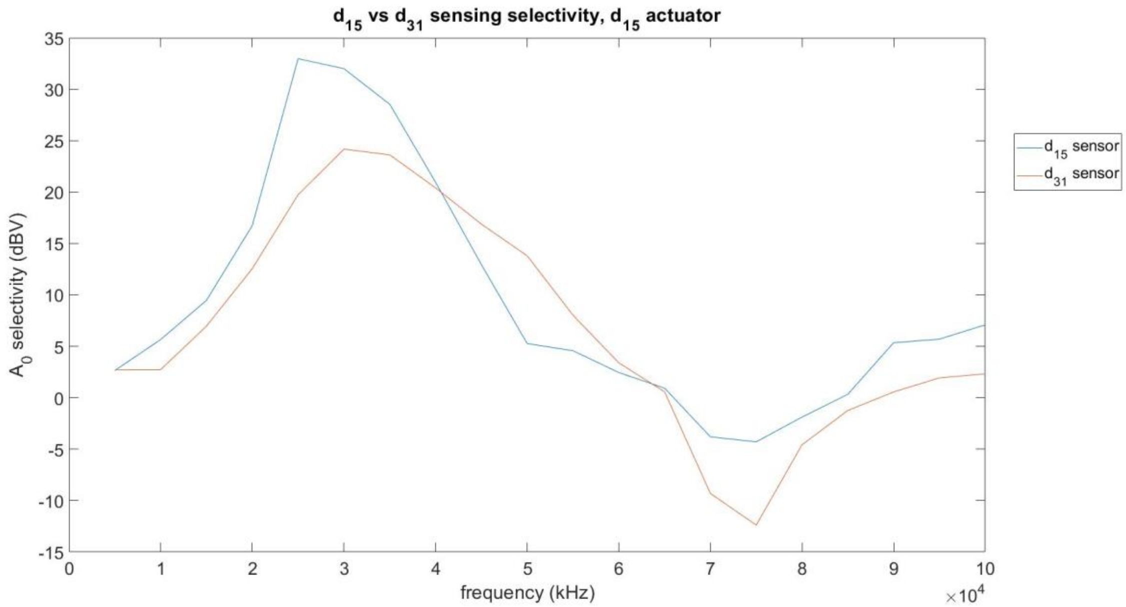

Figure 42: A_0 sensing selectivity of d_{15} and d_{31} PZT stimulated with d_{15} actuator. Composite sample.

The analysis was repeated using signals stimulated with a d_{15} actuator. The average A_0 selectivity for the d_{15}-to-d_{15} configuration and d_{15}-to-d_{31} configuration are 18.1 dBV and 12.7 dBV respectively. The d_{15} sensor shows an average of 5.40 dBV higher A_0 selectivity when stimulated with a neutral axis d_{15} actuator.

Table 4: A_0 sensing selectivity

	d_{15} sensing selectivity (dBV)	d_{31} sensing selectivity (dBV)	d_{15} advantage (dBV)
actuated with d_{31}	5.67	7.89	-2.22
actuated with d_{15}	18.1	12.7	5.4

Table 4 summarizes the reported A_0 sensing selectivity of the d_{31} and d_{15} PZTs. The d_{15} PZT is a more selective sensor when the Lamb waves originate from neutral axis d_{15} PZT. However, the d_{15} PZT performed worse as an A_0 selective sensor when the Lamb waves originated from a d_{31} PZT. It is suspected that this effect would not be seen if more consistent frequency sampling was used for both sets of actuator data.

5.0 Experimental Results Compared with Theory and Simulation

The experimental methods showed that the A_0 selectivity of a neutral axis d_{15} PZT is 12.7 dBV. The selectivity dropped to 8.68 dBV when the d_{15} PZT was moved from the neutral axis a distance of 5.5% of the sample's thickness. We would like to compare this to theory and the finite element simulation results. The previous graphs of theoretical and simulated power flow ratio were functions of both frequency and the PZT distance from the neutral axis. To remove the factor of frequency, the average powerflow ratio was calculated across all frequencies.

The theory and simulation were developed for a sample thickness of 3 mm. The carbon fiber composite sample which was used in experiment measured 4.5 mm. To overcome this discrepancy, the PZT distance from the neutral axis is reported in terms of percentage of the samples thickness.

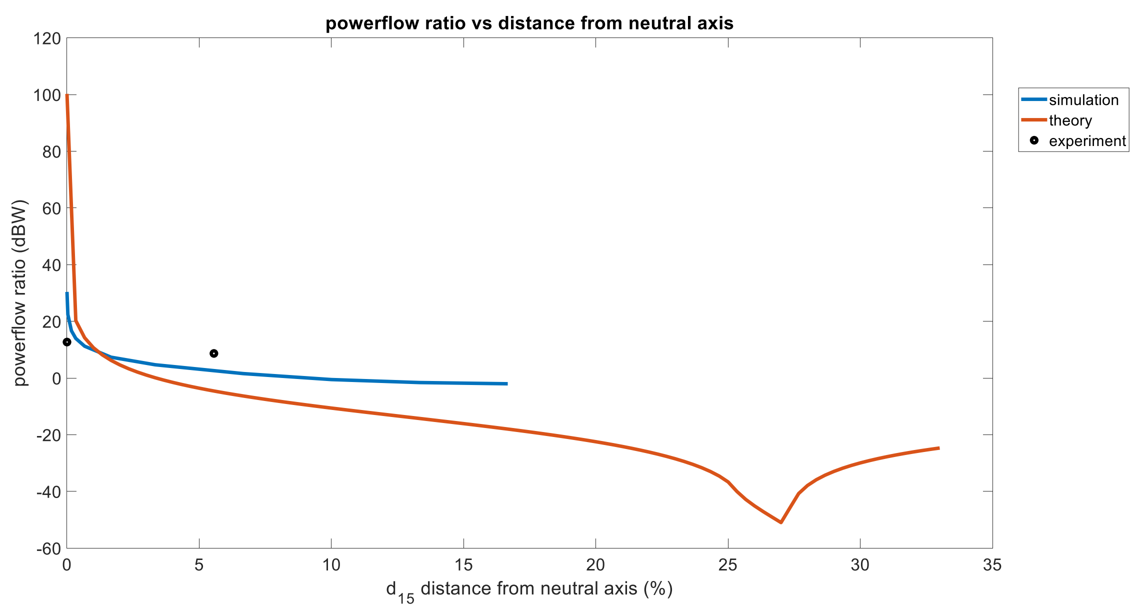

Figure 43: Comparison of theoretical, experimental, and simulated power flow ratio vs d_{15} distance from neutral axis

A comparison of the power flow ratio determined analytically, experimentally, and with simulation is shown in Figure 43. The slope of the simulation and theory curves is approximately the same. There is a large discrepancy between theory and simulation at the neutral axis, which predict 100 dB and 30 dB respectively. This is due to a singularity in the theoretical power flow ratio. According to theory, there should be no power flow due to the S_0 mode when the d_{15} PZT is at the neutral axis. Indeed, to overcome the singularity at the neutral axis, the theoretical powerflow ratio was reported instead for a d_{15} PZT located one nanometer from the neutral axis. Though the simulated S_0 power flow is very low at the neutral axis, it is not zero. Hence, the simulated power flow ratio at the neutral axis is a finite value.

The experimental power flow ratio at the neutral axis is 12.7 dB, which is substantially lower than both the theoretical and simulated values. Considering the steep decline shown in theory and simulation, it is entirely possible that the d_{15} PZT is not truly at the neutral axis of the structure. By interpolating on the simulation curve, we find the power flow ratio is 12.7 dB when the PZT is 0.5% of the thickness from the neutral axis. In the 4.5 mm thick sample, this corresponds to 22 microns. It seems reasonable that the d_{15} PZT in the composite sample could be as much as 22 microns from the neutral axis, and this would explain the discrepancy.

That said, the experimental power flow ratio at 5.5% is more distant from theoretical and simulated values. While the experimental power flow ratio at 5.5% is 8.68 dB, the theoretical power flow ratio is -4.5 dB. Interpolating from the simulation curve, we find the power flow ratio is 5.5% is 2.66 dB. In other words, with the PZT at 5.5% of the sample's thickness from the neutral axis, the experimental power flow ratio is within 69% of simulation. When the PZT is at the neutral axis, the experimental power flow ratio is within 58% of simulation.

There are a couple possible explanations for the differences between the simulations and theory. The theoretical analysis is quasi-static and assumes a uniformly distributed shear force along the top and bottom of the PZT. It does not account for the change in shape of the PZT as the voltage is applied. The finite element simulation is dynamic and allows for a varying shear force on the surfaces of the PZT. The shape of the PZT changes as the voltage is applied.

6.0 Conclusions

The objective of this research was to study the relationship between the through-thickness position of a d_{15} PZT embedded in plate-like structures on the actuation and sensing of A_0 and S_0 Lamb waves. An analytical approach was taken to determine the theoretical through-thickness displacement, shear strain, and axial power flow as a function of shear mode PZT distance from the neutral axis. A finite element model was constructed to verify the analytical functions which were derived, and study the frequency response of displacement, shear strain, and sensor voltage. Experiments were performed to study the S_0 and A_0 wave peak voltages as a function of d_{15} PZT distance from the neutral axis. Experiments were also performed to compare the peak voltage of signals actuated by neutral axis d_{15} PZTs with those actuated by surface mounted d_{31} PZTs, as well as compare the peak voltage of signals sensed by neutral axis d_{15} PZTs with those sensed by surface mounted d_{31} PZTs.

The significant findings that can be drawn from this work can be summarized as follows:

1. A neutral-axis shear-mode d_{15} PZT will selectively actuate the A_0 mode. At the neutral axis, the d_{15} PZT had an A_0 actuation selectivity of 12.7 dBV. A 4.02 dBV decrease in actuation selectivity was observed experimentally when the PZT was moved 5.5% of the sample's thickness away from the neutral axis, a rate of -0.73 dBV/%.
2. The A_0 actuation selectivity of a neutral axis d_{15} PZT was found to be 6.8 dBV, which was 1.6 dBV higher than a surface-mounted d_{31} PZT.

3. A neutral-axis shear-mode d_{15} PZT will selectively sense the A_0 mode. The A_0 sensing selectivity of a neutral axis d_{15} PZT was found to be 10 dBV, which was 3 dBV higher than a surface-mounted d_{31} PZT.
4. As an actuator, a neutral-axis shear-mode d_{15} PZT was found to produce a smaller strain wave than a surface mounted conventional d_{31} PZT for a given electric field strength. A d_{31} actuator created an average of 2 times the voltage of a d_{15} actuator, when measured with a d_{15} sensor. This was true for both A_0 and S_0 waves.
5. As a sensor, a neutral-axis shear-mode d_{15} PZT was found to produce a smaller voltage than a surface mounted conventional d_{31} PZT for a given strain wave. A d_{31} sensor created an average of 2 times the voltage of a d_{15} sensor, when stimulated with a d_{15} actuator. This was true for both A_0 and S_0 waves.
6. The d_{15} to d_{15} system produces 10 dBV greater selectivity than the traditional d_{31} to d_{31} system. In other words, for a desired A_0 peak amplitude, the neutral-axis d_{15} PZT system creates an S_0 signal that is 1/3 as large as the surface-mounted d_{31} PZT system.

Of course, there is potential for improvements to the current work, as well as further work that would build upon what has been studied here. The frequency response recorded in the finite element simulation had several peaks, while the theoretical frequency response had one or two. Many peaks existed in the experimental frequency response, though they did not match with simulation. It is possible that this discrepancy could be resolved by performing a harmonic analysis that uses a non-reflective boundary condition (NRB) [43]. This would eliminate the effect of constructive and destructive interference of waves bouncing off the edges of the plate as they reach the sensors.

More aluminum laminate samples should be constructed, and the experiment which was performed to draw conclusions 3 and 4 above should be repeated. Using more samples would reduce the possibility of unintentional off-axis position of the d_{15} PZT and increase confidence in the results.

More composite samples could be constructed, and the experiment which was performed to draw conclusion 1 above should be repeated. The d_{15} actuator could be placed at more intervals through the thickness of the structure. This would help establish the extent of A_0 selectivity drop as the PZT is moved from the neutral axis.

More data should be obtained at high frequencies to form a more comprehensive baseline for the surface-mounted d_{31}-to-d_{31} configuration, in order to gain confidence in conclusion 2 and 6.

Theory indicates that a long and thin shear-mode PZT will create a lower equivalent tensile strain, and thus a smaller S_0 wave, than a short and thick PZT. As the length-to-thickness ratio increases, the A_0 mode selectivity may increase. These experiments and simulations should be repeated with thinner PZTs to confirm this trend.

Appendix A: Comparison of Two Frequency Response Methods

The frequency response of the actuator-structure-sensor system was determined. A series of chirp signals was sent to the actuator, and the d_{15} sensor response was recorded. Table 5 shows the signal bandwidths, peak to peak voltages, and sweep times. A Fast Fourier transform was performed on the d_{15} sensor response to determine the natural frequencies of the system.

Natural frequencies were also determined using a Welch analysis. This method uses broadband white noise as an input. Ten volts peak-to-peak was used in this experiment. A Welch analysis has the advantage that it only needs 1 signal as an input, and thus only 1 measurement. The chirp signal must be split into several signals of smaller bandwidth to investigate the frequencies of interest, with each input signal requiring a separate measurement.

Table 5: Chirp Signal Specifications

Peak to Peak Voltage	Start Frequency	Stop Frequency	Sweep Time
10 V	1 kHz	10 kHz	0.2 s
10 V	10 kHz	100 kHz	0.2 s
10 V	100 kHz	1 MHz	0.2 s

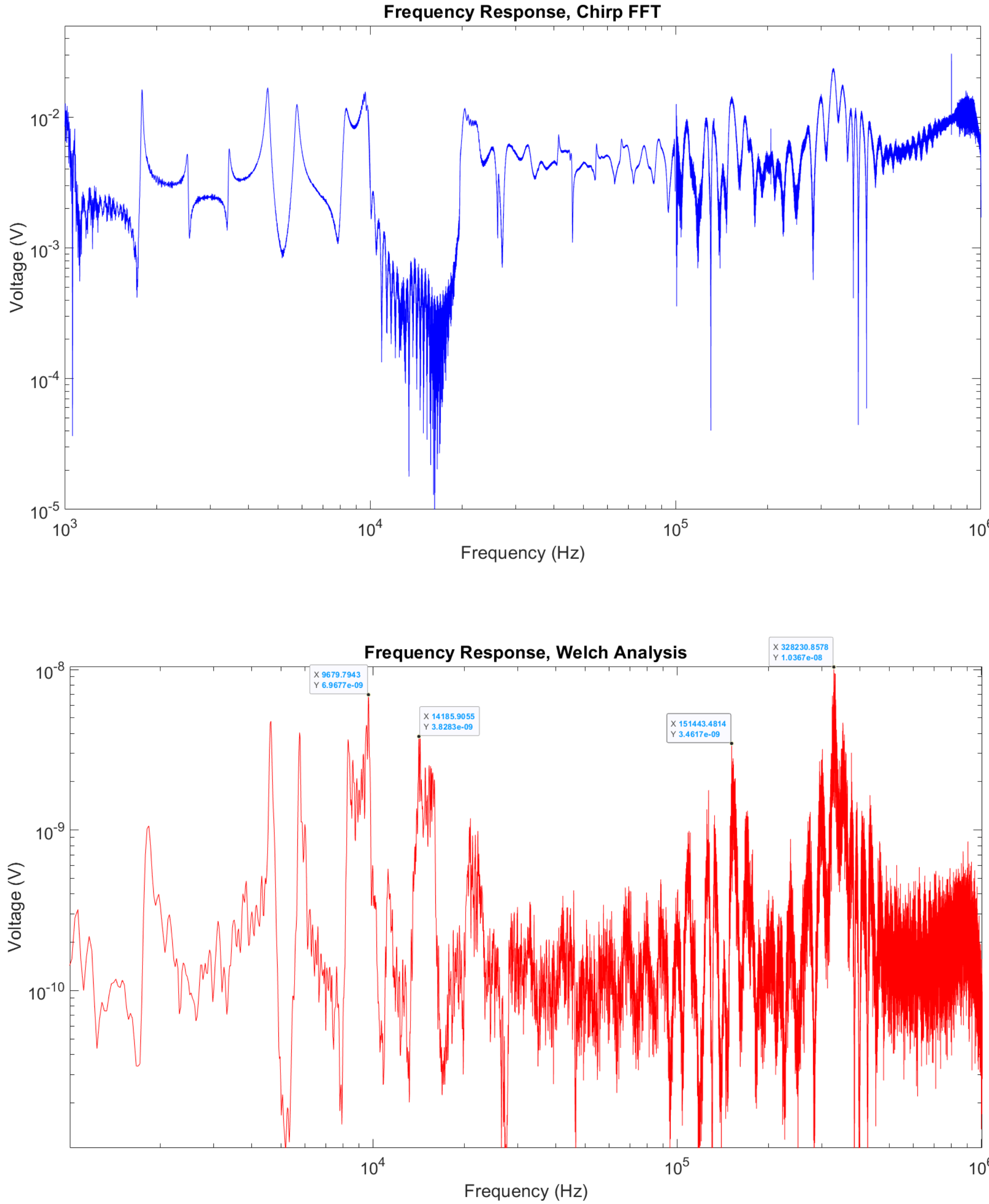

Figure 44: Frequency response via Chirp method and Welch analysis

A sample of four of the stronger natural frequencies are highlighted in the Figure 44. For each of these frequencies, a 5 peak Hanning-windowed toneburst was applied to the d_{15} actuator, and the voltage at the d_{15} and d_{31} sensors was recorded. Two of the resulting oscilloscope measurements are shown below.

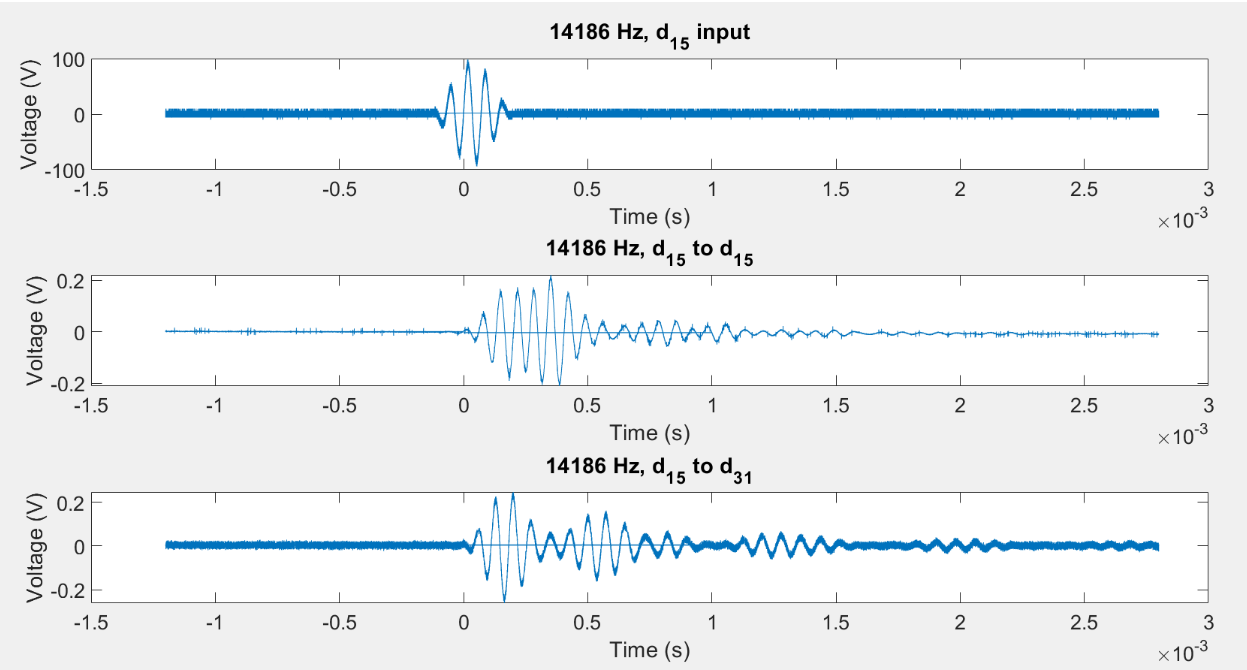

Figure 45: d_{15} and d_{31} sensor response to 14186 Hz toneburst. Aluminum sample.

Figure 45 shows a 100-volt peak-to-peak 14186 Hz toneburst applied to the d_{15} actuator, and the response at the d_{15} and d_{31} sensors. The d_{15} sensor response has a max amplitude of 400 mV peak-to-peak, and the d_{31} response is approximately the same. It is known that a shear mode PZT does not sense the S_0 Lamb wave mode. Since the actuation is below the necessary frequency-thickness product to actuate the A_1 mode, we know that the first wave arriving at the d_{15} sensor is the A_0 mode. The first wave of the d_{31} sensor arrives at the same time. Therefore, it is also the A_0 mode. S_0 waves travel faster than A_0 waves. Since the d_{31} sensor did not detect any waves arriving before the A_0 wave, it implies that there was no S_0 wave in the structure. In other words, a d_{15} actuator located at the neutral axis purely actuates the A_0 mode.

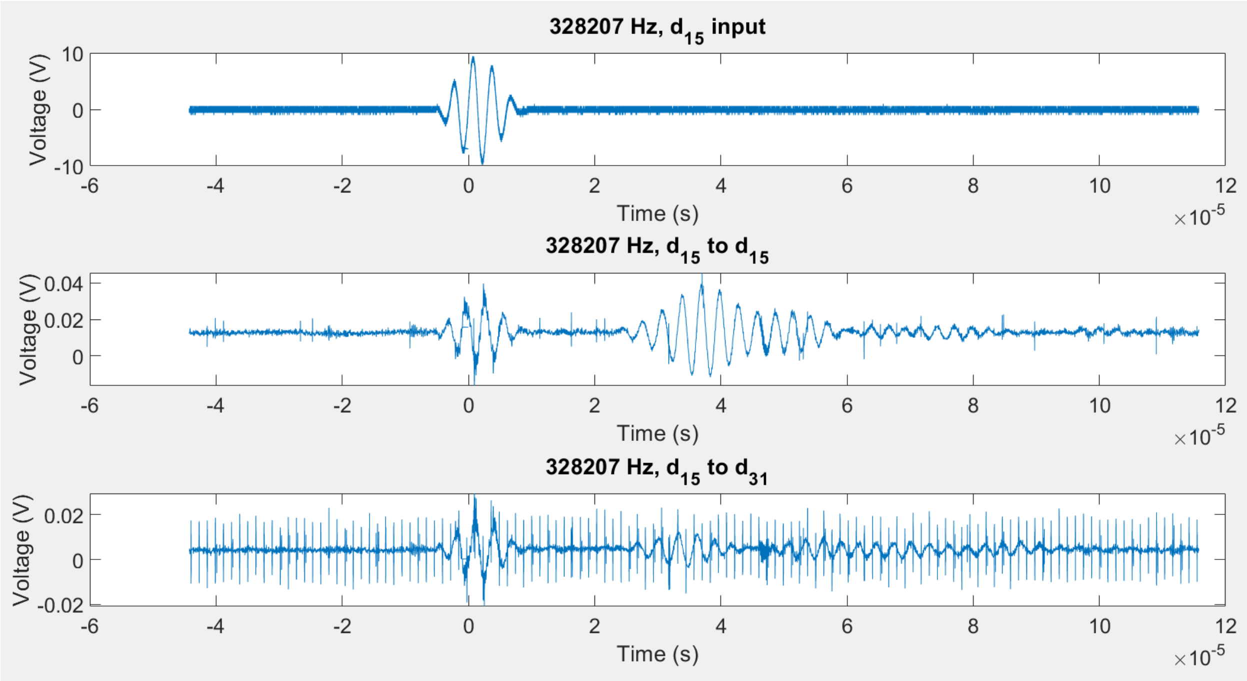

Figure 46: d_{15} and d_{31} response to 328207 Hz toneburst. Aluminum sample.

Figure 46 shows the response to a 10-volt peak-to-peak 328207 Hz toneburst. Unlike in the previous result, the sensors show an earlier response. Because it is at the same time as the actuator, it is likely the result of an electromagnetic wave and not a Lamb wave. This would explain the absence of the signal in the response to the lower frequency 14186 Hz toneburst. The max amplitude of the d_{15} signal is approximately 70 mV, while the max amplitude of the d_{31} signal is approximately 30 mV. Again, the first wave arrives simultaneously at the d_{15} and d_{31} sensors. The S_0 mode is absent.

Appendix B: d_{15} vs d_{31} Sensing Selectivity in Aluminum Sample

The methodology described in section 4.3.3 was used to find the A_0 selectivity of the d_{15} and d_{31} sensors. Tone-bursts were applied to the d_{15} and d_{31} actuator in turn, using the frequencies highlighted in Figure 32.

The selectivity is determined from the ratio of peak A_0 voltage to peak S_0 voltage. S_0 waves travel faster than A_0, so there is potential for an S_0 wave to reflect off the end of the sample and cause interference with the arriving A_0 wave. To reduce the effects of S_0 end reflections on the A_0 peak measurements, only the signals originating with a d_{15} actuator were considered. A d_{15} PZT located at the neutral axis should not actuate the S_0 mode, so there is less opportunity for a S_0 reflection to interfere with the A_0 mode. However, the aluminum sample's epoxy layer measured 1.5 mm thick, while the d_{15} actuator measured 1 mm. The d_{15} actuator could be much as 0.25 mm off the neutral axis. While S_0 actuation with the d_{15} PZT is possible in this case, it is likely less severe than with the surface mounted d_{31}.

The peak voltages in signals actuated by a d_{15} PZT and sensed by the d_{15} and d_{31} PZTs are shown in Table 6. The RMS amplitude of the noise is reported as well.

Table 6: d_{15} actuator peak voltages. Aluminum sample.

frequency (Hz)	d15 S0 peak (mV)	d15 A0 peak (mV)	d15 noise floor (mV)	d31 S0 peak (mV)	d31 A0 peak (mV)	d31 noise floor (mV)	d15 A0/S0 selectivity (dBV)	d31 A0/S0 selectivity (dBV)
43300	14.1	22.0	5.60	35.7	21.3	6.70	3.88	-4.47
53900	22.8	25.7	5.50	69.2	37.6	6.80	1.03	-5.31
85000	16.8	23.2	5.70	43.5	38.0	6.80	2.80	-1.17
95800	14.2	25.0	5.80	39.1	73.5	7.06	4.89	5.48
113829	13.8	22.1	4.80	33.9	107	6.31	4.07	9.97

The voltages from the d_{31} sensors are larger than the d_{15} sensors (approximately twice the voltage). This is consistent with the simulation. The d_{15} sensors are shown to be more selective to the A_0 mode (up to 8 dBV more selective). However, at 95800 Hz and 113829 Hz the d_{31}

sensor has higher A_0 selectivity. It is suspected that this is due to an artificially high A_0 peak voltage, an effect of constructive interference from an S_0 end reflection. To increase confidence in these results, the experiment was repeated on a composite sample of the same geometry, and the number of sampled frequencies was increased.

References

[1] M. B. Rao, M. R. Bhat, C. R. L. Murthy, K. V. Madhav and S. Asokan, "Structural Health Monitoring (SHM) Using Strain Gauges, PVDF Film and Fiber Bragg Grating (FBG) Sensors: A Comparative Study," in *National Seminar on Non-Destructive Evaluation*, Hyderabad, 2006.

[2] P. Cawley, "Structural health monitoring: Closing the gap between research and industrial deployment," *Structural Health Monitoring,* vol. 17(5), pp. 1225-1244, 2018.

[3] J.-B. Ihn and F.-K. Chang, "Detection and monitoring of hidden fatigue crack growth using a built-in piezoelectric sensor/actuator network: I. Diagnostics:," *Smart Materials and Structures,* vol. 13, pp. 609-620, 2004.

[4] *Guidelines for implementation of structural health monitoring on fixed wing aircraft*, SAE International, ARP6461, 2013.

[5] X. Qing, W. Li, Y. Wang and H. Sun, "Piezoelectric Transducer-Based Structural Health Monitoring for Aircraft Applications," *Sensors,* vol. 19, no. 545, 2019.

[6] "Distributed Fiber Optic Strain and Temperature Sensing for Structural Health Monitoring".

[7] K. Wang, W. Cao, L. Xu, X. Yang, Z. Su and X. Zhang, "Diffuse ultrasonic wave-based structural health monitoring for railway turnouts," *Ultrasonics,* vol. 101, February 2020.

[8] C. C. Ciang, J.-R. Lee and H.-J. Bang, "Structural health monitoring for a wind turbine system: a review of damage detection methods," *Measurment Science and Technology,* vol. 19, 2008.

[9] *Mao Z. Slides on bridge monitoring in China part of presentation by C.R Farrar, http://engineering.unl.edu/images/events/BBD/Nebraska%202015.pdf.*

[10] X. Zhu and P. Rizzo, "Sensor array for the health monitoring of truss structures by means of guided ultrasonic waves," *Journal of Civil Structural Health Monitoring,* vol. 4, pp. 221-234, 2014.

[11] W. S. Na, "Possibility of detecting wall thickness loss using a PZT based structural health monitoring method for metal based pipeline facilities," *NDT&E International,* vol. 88, pp. 42-50, 2017.

[12] P. S. Tua, S. T. Quek and Q. Wang, "Detection of cracks in cylindrical pipes and plates using piezo-actuated Lamb waves," *Smart Materials and Structures,* vol. 14, pp. 1325-1342, 2005.

[13] Z. Chang and A. Mal, "Scattering of Lamb waves from a rivet hole with edge cracks," *Mechanics of Materials,* vol. 31, pp. 197-204, 1999.

[14] S. S. Kessler, S. M. Spearing and C. Soutis, "Damage detection in composite materials using Lamb wave methods," *Smart Materials and Structures,* vol. 11, pp. 269-278, 2002.

[15] F. L. Degertekin and B. T. Khuri-Yakub, "Lamb Wave Excitation by Hertzian Contacts with Applicationsin NDE," *IEEE Transactions on Ultrasonics, Ferroelectrics, and Frequency Control,* vol. 44, no. 4, pp. 769-779, 1997.

[16] E. A. Birt, "Damage detection in carbon-fibre composites using ultrasonic Lamb waves," *Insight,* vol. 40, no. 8, pp. 335-339, 1998.

[17] P. Huthwaite, R. Ribichini, P. Cawley and M. J. Lowe, "Mode Selection for Corrosion Detection in Pipes and Vessels via Guided Wave Tomography," *IEEE Transactions on Ultrasonics, Ferroelectrics, and Frequency Control,* vol. 60, no. 6, pp. 1165 - 1177, 2013.

[18] V. Giurgiutiu, "Tuned Lamb Wave Excitation and Detection with Piezoelecric Wafer Active Sensors for Structural Health Monitoring," *Journal of Intellegent Material Systems and Structures,* vol. 16, April 2005.

[19] S. Grondel, C. Paget, C. Delebarre, J. Assaad and K. Levin, "Design of optimal configuration for generating A0 Lamb mode in a composite plate using piezoceramic transducers," *The Journal of the Acoustical Society of America,* vol. 112, no. 1, pp. 84 - 90, 2002.

[20] T. Clarke, F. Simonetti, S. Rohklin and P. Cawley, "Development of a Low-Frequency High Purity A0 Mode Transducer for SHM Applications," *IEEE Transactions on Ultrasonics, Ferroelectrics, and Frequency Control,* vol. 56, no. 7, pp. 1457 - 1468, 2009.

[21] R. G. Budynas and J. K. Nisbett, Shigley's Mechanical Engineering Design, 10 ed., New York, NY: McGraw-Hill Eductation, 2015.

[22] J. S. Chilles, A. F. Koutsomitoploulou, A. J. Croxford and I. P. Bond, "Monitoring cure and detecting damage in composites with embedded sensors," *Composites Science and Technology,* vol. 134, pp. 81-88, 2016.

[23] S. Masmoudi, A. E. Mahi and S. Turki, "Use of piezoelectric as acoustic emission sensor for in situ monitoring of composite structures," *Composites Part B*, vol. 80, pp. 307-320, 2015.

[24] J. S. Chilles, A. Croxford and I. P. Bond, "Design of an embedded sensor, for improved structural performance," *Smart Materials and Structures*, vol. 24, no. 11, 2015.

[25] C. T. Sun and X. D. Zhang, "Use of thickness-shear mode in adaptive sandwich structures," *Smart Materials and Structures*, vol. 4, pp. 202 - 206, 1995.

[26] A. Benjeddou, M. A. Trinidade and R. Ohayon, "Piezoelectric actuation mechanisms for inteligent sandwich structures," *Smart Materials and Structures*, vol. 9, pp. 328-335, 2000.

[27] S. S. Vel and R. C. Batra, "Exact Solution for Rectangular Sandwich Plates with Embedded Piezoelectric Shear Actuators," *AIAA Journal*, vol. 39, no. 7, pp. 1363 - 1373, 2001.

[28] H. Altammar, A. Dhingra and N. Salowitz, "Ultrasonic Sensing and Actuation in Laminate Structures Using Bondline-Embedded d35 Piezoelectric Sensors," *Sensors*, vol. 18, pp. 3885 - 4005, 2018.

[29] A. Benjeddou and J.-F. Deu, "Piezoelectric Transverse Shear Actuation and Sensing of Plates, Part 1: A Three-Dimensional Mixed State Space Formulation," *Journal of Intelligent Material Systems and Structures*, vol. 12, pp. 435 - 449, 2001.

[30] A. Benjeddou and J.-F. Deu, "Piezoelectric Transverse Shear Actuation and Sensing of Plates, Part 2: Application and Analysis," *Journal of Intellegent Material Systems and Structures*, vol. 12, pp. 451-467, 2001.

[31] V. Giurgiutiu, Structural health monitoring with piezoelectric wafer active sensors, 2 ed., Amsterdam: AP, Academic Press/Elselvier, 2014.

[32] "LOCTITE EA 9394: Epoxy Paste Adhesive; Henkel Corporation Aerospace: Bay Point, CA, USA, 2013.".

[33] *Matlab. Natick, MA, USA: Mathworks, 2020..*

[34] *M. Lowe and B. Pavlakovic, Disperse. London, UK: Imperial College NDT Lab, 2020. Available from: http://www.imperial.ac.uk/non-destructiveevaluation/.*

[35] K.-J. Bathe, Finite Element Procedures, 2 ed., Watertown, MA: Prentice Hall, Pearson Educcation, Inc., 2014.

[36] *Chemtronics Technical Data Sheet: 60 Minute Conductive Epoxy; Chemtronics: Kennesaw, GA, USA, 2008..*

[37] *Yang, J. Analysis of Piezoelectric Devices; World Scientific Publishing Co. Pte. Ltd.: Singapore, 2006; ISBN 978-981-256-861-8..*

[38] *Physical and Piezoelectric Properties of APC Materials; APC International Ltd.: Mackeyville, PA, USA, 2017..*

[39] "33500B Series Waveform Generators; Keysight Technologies, Inc.: Santa Rosa, CA, USA, 2017.".

[40] "Model 7600M/7602M Wideband Power Amplifiers; Krohn-Hite Corporation: Brockton, MA, USA, 2004.".

[41] "MDO 3000 Series Mixed Domain Oscilloscope; Tektronix, Inc.: Beaverton, OR, USA, 2003.".

[42] *FibreGlast Technical Data Sheet: 2214 Prepreg 4.3 oz IM Unidirectional Fabric 6-Month; Fibre Glast Developments Corporation: Brookville, OH, USA, 2020.*

[43] Y. Shen and V. Giurgiutiu, "Effective non-reflective boundary for Lamb waves: Theory, finite element implementation, and applications," *Wave Motion,* vol. 58, pp. 22-41, 2015.